UC Irvine

UC Irvine Electronic Theses and Dissertations

Title

Spatial, temporal, and spectral control towards quantitative tissue spectroscopic imaging in the spatial frequency domain

Permalink

https://escholarship.org/uc/item/7v206815

Author

Torabzadeh, Mohammad

Publication Date

2018

Copyright Information

Peer reviewed|Thesis/dissertation

UNIVERSITY OF CALIFORNIA,
IRVINE

Spatial, Temporal, and Spectral Control towards Quantitative Tissue Spectroscopic
Imaging in the Spatial Frequency Domain

DISSERTATION

submitted in partial satisfaction of the requirements
for the degree of

DOCTOR OF PHILOSOPHY

in Biomedical Engineering

By

Mohammad Torabzadeh

Dissertation Committee:
Professor Bruce J. Tromberg, Chair
Professor Anthony J. Durkin
Professor Bernard Choi

2018

DEDICATION

To

my beloved mother, father, and first-grade teacher

"The breath of the flute player:

does it belong to the flute?"

-Rumi

Table of Contents

List of figures

List of equations

List of symbols/abbreviations

Symbol	Meaning
A	reduced scattering pre-factor
b	reduced scattering slope
C	Fourier coefficient matrix
CS	Compressed Sensing
FFT	fast Fourier transform
f_x	spatial frequency
λ	wavelength
μ_a	absorption coefficient
μ_s'	reduced scattering coefficient
I	raw intensity
M	modulated (AC) term in SFDI intensity
AC	alternating current (modulated illumination)
CCD	charge coupled device
DAQ	data acquisition
DC	direct current (planar illumination)
DMD	digital micromirror device
DLP	digital light projector
FOV	field-of-view
FPS	frames per second
LED	light emitting diode
NIR	near infrared
ROI	region of interest

Symbol	Meaning
sCMOS	scientific-grade complementary metal-oxide semiconductor
SFD	spatial frequency domain
SFDI	Spatial Frequency Domain Imaging
SLM	spatial light modulator
MTF	modulation transfer function
SNR	signal-to-noise ratio
StO_2	tissue oxygen saturation
SWIR	short wave infrared
μM	micromolar

Acknowledgements

Curriculum Vitae

Mohammad Torabzadeh

2013   B.S. in Mechanical Engineering, University of Tehran

2016   M.S. in Biomedical Engineering, University of California, Irvine

2018   Ph.D. in Biomedical Engineering, University of California, Irvine

FIELD OF STUDY

Biophotonics

PUBLICATIONS

1. **Torabzadeh, M.**, Park, I. Y., Bartels, R. A., Durkin, A. J., and Tromberg, B. J. (2017). Compressed single pixel imaging in the spatial frequency domain. Journal of Biomedical Optics, 22(3), 030501-030501.

2. **Torabzadeh, M.**, Stockton, P. A., Kennedy, G. T., Saager, R. B., Bartels, R. A., Durkin, A. J., Tromberg, B. J. Hyperspectral imaging in the spatial frequency domain with a supercontinuum source. In preparation for submission to Journal of Biomedical Optics.

3. **Torabzadeh, M.**, Stockton, P. A., Kennedy, G. T., Saager, R. B., Bartels, R. A., Durkin, A. J., and Tromberg, B. J., Hyperspectral characterization of tissue simulating phantoms using a supercontinuum laser in a spatial frequency domain imaging instrument, In Proceedings of SPIE Photonics West, January 2018, San Francisco, USA.

4. Wilson, R. H., Crouzet, C., **Torabzadeh, M.**, Bazrafkan, A., Farahabadi, M. H., Jamasian, B., Donga, D., Alcocer, J., Zaher, S. M., Choi, B., Akbari, Y., and Tromberg, B. J. (2017). High-speed spatial frequency domain imaging of rat cortex detects dynamic optical and physiological properties following cardiac arrest and resuscitation. Neurophotonics 4(4).

PRESENTATIONS

5. **Torabzadeh, M.**, Park, I.Y., Durkin A.J., and Tromberg, B.J., Multispectral compressed single pixel imaging in the spatial frequency domain, SPIE Photonics West, January 2017, San Francisco, USA.

6. **Torabzadeh M.**, Nadeau, K. P., Durkin, A. J., and Tromberg, B. J., Real-time processing and visualization of spatial frequency domain images, SPIE Photonics West, February 2016, San Francisco, USA.

7. **Torabzadeh, M.**, Stockton, P. A., Kennedy, G. T., Saager, R. B., Bartels, R. A., Durkin, A. J., and Tromberg, B. J., Hyperspectral characterization of tissue simulating phantoms using a supercontinuum laser in a spatial frequency domain imaging instrument, SPIE Photonics West, January 2018, San Francisco, USA.

8. **Torabzadeh, M.**, Stockton, P. A., Yazdi, H. S., Kennedy, G. T., Saager, R. B., Bartels, R. A., Durkin, A. J., Tromberg, B. J., Broadband spatial frequency domain imaging using a supercontinuum laser source, UC Systemwide Bioengineering Symposium, June 2018, Riverside, USA.

9. **Torabzadeh, M.**, Wilson, R. H., Crouzet, C., Bazrafkan, A., Akbari, Y., Choi B., Tromberg, B. J., High speed imaging of cerebral oxygenation and blood flow during cardiac arrest and resuscitation, 14th Annual Congress of Society of Brain mapping and Therapeutics, April 2018, Los Angeles, USA.

Abstract of the Dissertation

Spatial, temporal, and spectral control towards quantitative tissue spectroscopic imaging in the spatial frequency domain

By

Mohammad Torabzadeh

Doctor of Philosophy in Biomedical Engineering
University of California, Irvine 2018

Professor Bruce J. Tromberg, Chair

Spatial Frequency Domain Imaging (SFDI) is a non-contact wide-field spectroscopy technique that employs sinusoidal patterns of spatially modulated light as the excitation source. By obtaining the effective modulation transfer function of the diffusively reflected light from a turbid medium, it considers the contribution of reduced scattering and absorption coefficient to this function allowing for decoupling of the optical properties. The extracted optical properties at several wavelengths can provide quantitative information on concentration of tissue chromophores such as hemoglobin, fat, and water. It also delivers information on the arrangement of tissue structural components, mainly cells and extracellular matrix proteins. The technique has been utilized to investigate many phenomena in brain, kidney, and skin tissues.

Enhancing spatial, temporal, and spectral information content in SFDI can give insight to tissue constituents, their dynamics, and distribution. In this work, we developed and validated three variations of SFDI instruments with design considerations to match specific applications:

1. High Speed SFDI instrument that detects rat cortex dynamic optical and physiological properties at 17 frames per second following cardiac arrest and resuscitation.

2. Hyperspectral SFDI instrument which measures tissue optical properties at 1000 spectral bins over a broad range, 580-950 nm, and can spatially resolve concentrations of oxy- deoxy- and met-hemoglobin as well as water and fat fractions. It utilizes principles of spatial scanning of the spectrally dispersed output of a supercontinuum laser.

3. Single pixel SFDI instrument which takes advantage of high bandwidth available for spectral encoding using a single-element detector and sparse sampling based on compressed sensing to characterize tissue optical properties over a wide field of view, 35 mm × 35 mm.

Chapter 1

1. Introduction

Optical Imaging is a rising technology that has shown great potential in many disease prevention strategies, early detection interventions, and treatment monitoring [1]. This has been driven by advances in bio photonics (photon interactions in a biological environment), optoelectronics, and genetics. Living tissue is a dynamic environment in terms of metabolism and mechanical structure. Many diseases including diabetes, heart disease, and brain trauma can lead to changes in oxygen utilization ,water concentration, and tissue organization [2-9].

Diffuse Optical Imaging (DOI) is a non-invasive technique that gives insight on tissue structure and function, the basis of health and disease. DOI is conventionally performed in the near infrared regime (600-1000nm) allowing for deeper penetration depth. DOI can detect exogenous contrast agents such as fluorescent molecules and endogenous molecules (chromophores) such as oxygenated and deoxygenated hemoglobin, lipid, and water. It also delivers information on the arrangement of tissue structural components, mainly cells and extracellular matrix proteins.

DOI considers for the contribution of tissue bulk optical properties, scattering and absorption, in the detected signal on the sensor side by modulating the characteristics of light source. There are several techniques to separate absorption from scattering including time resolved [10], temporal frequency domain [11, 12], and spatial frequency domain [13].

In this work, we focus on the spatial frequency domain techniques. Spatial Frequency Domain Imaging (SFDI) is a non-contact wide-field spectroscopy technique that employs sinusoidal patterns of spatially modulated light as the excitation source. By obtaining the effective modulation transfer function of the diffusively reflected light from a turbid medium, it takes into account the

contribution of reduced scattering, μ_s', and absorption coefficient, μ_a, to this function allowing for decoupling of the optical properties [14, 15]. The extracted optical properties at several wavelengths can provide quantitative information on concentration of tissue chromophores such as oxy/deoxyhemoglobin and water. The technique has been utilized to investigate many dynamic phenomena in brain, kidney, and skin tissues [16-18].

1.1 Motivation for enhancing SFDI Information Content

There is a tradeoff between the spectral, spatial, and temporal resolution in the previously reported SFD techniques. The wide-field quantitative SFDI was first performed at several discrete wavelengths and spatial frequencies in the sub-minute regime [14, 19]. Other approaches utilized a broad-band light source and fiber-coupled spectrometer with a relatively small field of view (2 mm×2 mm spot size) to acquire finer spectral resolution [20]. SFDI has been developed using a image mapping spectrometer at 38 wavelengths at the frame rate of 5 Hz to characterize rat somatosensory cortex [21] and has been combined with a hyperspectral line-scan camera to image drug deposition in a rat model [22] at 0.2 Hz.

Figure 1.1 shows a plot of frame rate vs number of wavelength of SFDI instruments for 14 previously published studies. While the majority of instrument operate using less than 10 wavelengths and take several seconds to acquire a full data stack, there are studies that try to push instrumentation in one direction, either temporal or spectral resolution. There is tradeoff between spectral and temporal resolution since adding more wavelength using time multiplexing techniques proportionally decreases the acquisition rate.
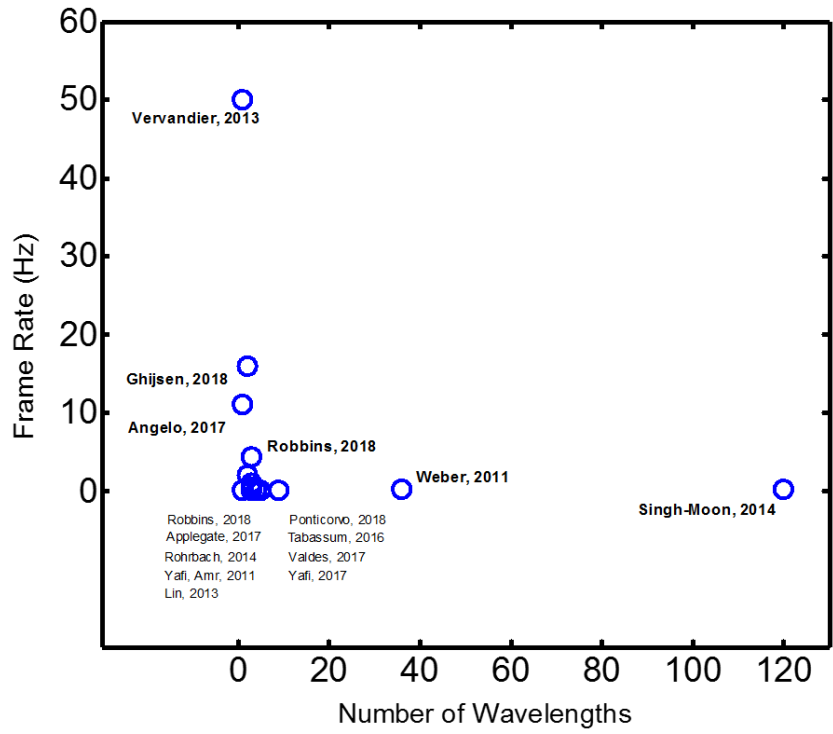
Figure 1.1 Frame rate and number of wavelength in previous SFDI studies

One of the main motivations to get acquire SFDI data faster is to mitigate the effect of motion artifacts from the sample. The motion artifact can arise mainly from breathing. Figure 1.2 shows effect of breathing artifact in a porcine burn model where there are fringes in the deoxyhemoglobin maps. Since SFDI patterns are projected sequentially onto the sample, changes in height of the sample due to breathing causes fringes in the demodulated reflectance maps which eventually propagates to oxygenation maps.
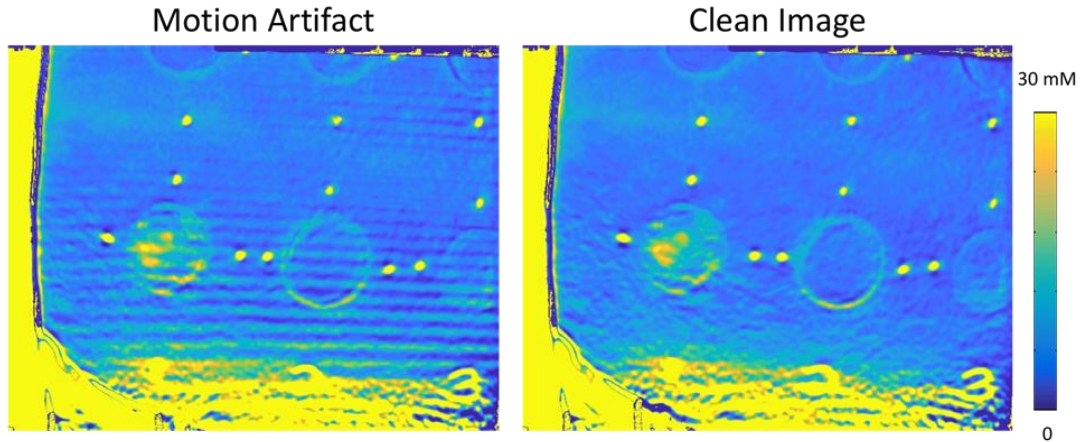
Figure 1.2 Effect of motion artifact in pig burns. Maps of deoxyhemoglobin 30 minutes after the burn.

Another motivation to acquire SFDI data at high temporal rates is to resolve dynamic physiological phenomenon. An example of which is [17] where a porcine model of renal occlusion is performed. There is drastic changes in renal oxygenation followed by the occlusion and release that cannot be captured a SFDI instrument with acquisition times of several seconds. A previous study in [23] utilizes a high speed SFDI instrument running at 33 Hz with 3 wavelengths and two spatial frequenting to capture dynamic hear beat signals from a human subject. The studies emphasize the importance of development and validation of SFDI instrument with high temporal and spectral resolutions.

In **Chapter 2**, we will discuss the implementation of a high-speed SFDI instrument to a preclinical animal model for cardiac arrest and resuscitation. In **Chapter 3**, we introduced a method for quantitative hyperspectral imaging (HSI) in the spatial frequency domain (hs-SFDI) to quantitatively image tissue optical properties, absorption (μ_a) and reduced scattering (μ'_s) coefficients, over a broad spectral range. The instrument utilizes principles of spatial scanning of the spectrally dispersed output of a supercontinuum laser projected onto a digital micromirror device (DMD) for sinusoidal pattern projection.

In **Chapter 4,** we compressed both spatial and spectral information in a SFDI setup to mitigate the trade-off between temporal and spectral resolution. We explored single pixel imaging based on sparse sampling, an evolving technology in biomedical imaging, which replaces 2-dimensional arrays of pixels with single pixel photodetectors, making the technique relatively inexpensive in terms of detector cost in the near infrared and short wave infrared region. The high temporal bandwidth of the photodiode is used to encode multiple excitation sources in time. Here, we present the design of a SFDI setup that employs a single-pixel camera on the detection side and a three-wavelength LED source. The extension of this work to a spectrometer-based setup allowed for hyperspectral compressed sensing SFDI.

Chapter 2

2. High Speed Spatial Frequency Domain Imaging

This chapter is derived from the publication [24].

2.1   Introduction

There are 500,000 cardiac arrest patients in United States every year and the mortality rate post resuscitation is high. One of the key medical problems is that very small percentage of people who survive cardiac arrest end up with favorable neurological outcome and very few achieve complete cerebral and neurological function. It's been shown that the degree of long term brain damage that survivors of cardiac arrest suffer is closely linked to the extent which cerebral vasculature recovers following resuscitation. This vascular damage and recovery can be sensed by our optical imaging techniques that interrogate cerebral blood flow and tissue oxygenation.

Spatial Frequency Domain Imaging (SFDI) is a quantitative, non-contact imaging technique that gives information about tissue two distinct optical properties, absorption and scattering. These two properties can be directly translated to tissue oxygenation and structural features, respectively. In this study, the aim was to monitor highly dynamic changes in the brain of a rodent during cardiac arrest and resuscitation.

To capture dynamic features in the brain, SFDI needs to be performed at high speed. Conventional SFDI instruments project sinusoidal patterns onto the sample which cannot be synchronized with high acquisition rates in the camera. Therefore, we introduced a novel projection technique based on high frequency square waves that allows for running both the Digital Micromirror (DMD) projector and the camera at 167 frames per second. Since SFDI measurements were performed at three wavelengths two spatial frequencies, we were able to capture 14 oxygen saturation and

oxy/deoxyhemoglobin maps per second. We incorporated our SFDI technology in an animal

Intensive Care Unit (ICU). The rodent in this experiment is treated the way a patient in ICU would

be treated. The rodent was continuously monitored with Electroencephalography (EEG), which

gives information about brain's electrical activity, in addition to our multimodal non-contact

optical imaging setup which interrogates brain tissue oxygenation, blood flow, and metabolism.

2.2   Materials and Methods

2.2.1   Version 1

The high speed SFDI instrument used in this study has three main components, a light engine with

a LED bank, a DMD projector which projects spatially modulated light onto the sample and a

camera which detects back scattered light emitted from the sample. The light engine (LumiBright

TM PR 2910A-100; Innovations in Optics, Woburn, MA) contains 12 LED bins for visible and

near infrared wavelengths. For this study, two G2 (655 nm, 230 mW), two H7 (730 nm, 118 mW),

and three K1 (850 nm, 62.1 mW) LEDs were used. The sCMOS camera (ORCA-Flash 4.0 V2,

Hamamatsu Photonics K.K., Japan) acquired images at 128x128 pixel resolution with a frame rate

of 167 Hz. An Arduino Due microcontroller (Sparkfun Electronics, Niwot, CO) synchronized the

LEDs, camera, and light engine as shown in Figure 2.1. By running the camera in External Edge

Trigger mode, each exposure was initiated by a Transistor-Transistor Logic (TTL) pulse from the

Arduino. The camera then sent a TTL pulse back to the Arduino after the exposure ended. The

Arduino used the rising edge of this pulse to externally trigger the LED bank and the DMD,

switching serially between the different wavelengths and projection patterns. The frame rate of the

camera depends on pixel resolution (128×128), exposure time (1 ms), and running mode (External

Edge Trigger). We also considered delay times to compensate for the rise time of the LEDs and

pattern refresh period of the DMD. These delay times and camera parameters provided an overall frame rate of 167 Hz.

The maximum 8-bit pattern refresh rate on the DMD is 60 Hz which is less than frame rate of the camera. To resolve this issue, instead of 8-bit sinusoidal patterns, square-wave spatial frequency patterns are used. The refresh rate for binary square-waves is 5 kHz. The patterns are offloaded to the projector software. This enables higher SFDI acquisition rate as compared to sinusoidal pattern projections. The projection sequence consists of a zero-spatial frequency pattern, planar illumination, followed by three $2\pi/3$-shifted square waves at spatial frequency of 0.3 mm^{-1}. This sequence is repeated for each wavelength which results in a stack of 12 frames. Therefore, optical properties at each wavelength are extracted at $167/12 \simeq 14$ Hz. Since a relatively high spatial frequency of square waves is used (0.3 mm^{-1}) and tissue acts as a low pass filter in spatial frequency domain. Reflected square waves can be approximated as sinusoidal patterns and the conventional three phase demodulation technique can be implemented without considerable artifacts from attenuated higher harmonics of the square wave [25]. Once the raw images are demodulated and calibrated against a tissue phantom with known optical properties, calibrated diffuse reflectance is fitted using a Montel Carlo model of photon transport in turbid medium to yield absorption and reduced scattering maps at three wavelengths. Absorption at each pixel can then be fitted to extinction coefficient of two dominant chromophores in the sample. Oxygen saturation is then defined as ratio of oxyhemoglobin concentration over the sum of oxy and oxyhemoglobin concentrations.

Figure 2.1 The high-speed SFDI and LSI instruments (Version 1)

2.2.2 Rodent ICU

To demonstrate the significate of the high speed SFDI instrument to quantify dynamic physiological process in brain tissue, an animal study is designed. The protocol has been approved by the Institutional Animal Care and Use Committee at the University of California, Irvine (protocol number 2013-3098). Details on animal preparation, cardiac arrest procedure, and cardiopulmonary resuscitation has been described in [26]. Briefly, a male Wister rat is anesthetized with isoflurane, intubated via trachea, and a breathing is mechanically controlled using a ventricular system. To monitor blood pressure on the arterial line and administer drugs, femoral artery is cannulated. A 4 mm × 6 mm craniectomy is performed on the right hemisphere atop the cortex to expose the skull for our optical imaging modality. Figure 2.2 shows the high-speed SFDI-LSI instrument integrated to the rodent ICU setup.

9
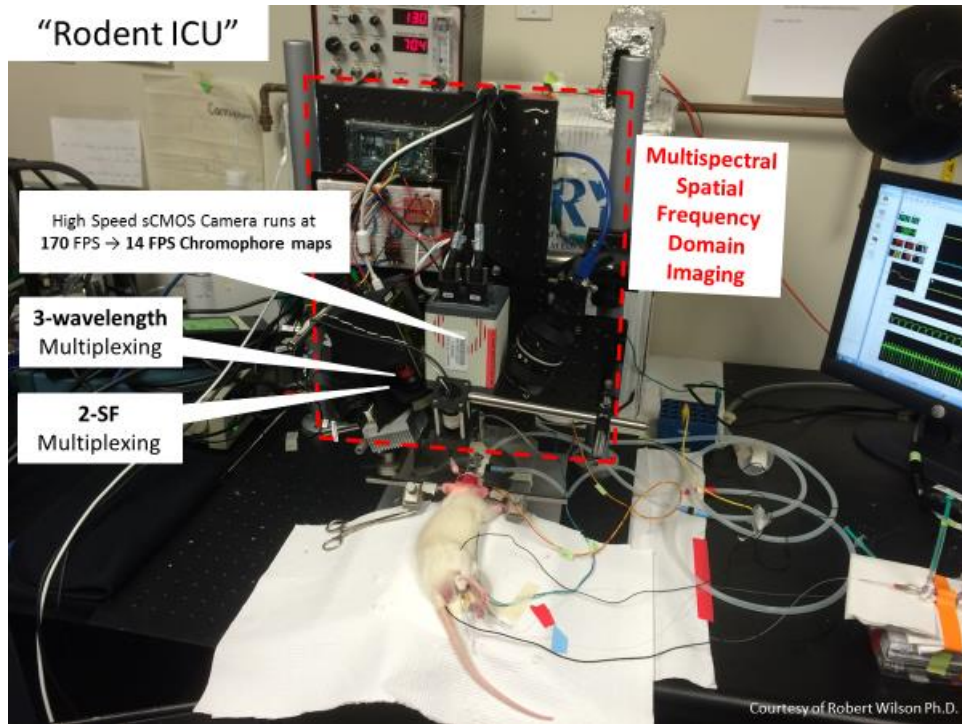
Figure 2.2 High Speed SFDI-LSI instrument integrated to the rodent ICU setup

2.2.3 Version 2

The first version of the high speed SFDI instrument suffered from low SNR for the 850nm wavelength reflectance, thus affecting the quality of Oxyhemoglobin maps. On the modified, we replaced the light engine with high power LEDs. Three LEDs where chosen: Thorlabs M660L2, 660nm, 940 mW, 1500 mA, Thorlabs M730L4, 730nm, 515 mW, 1200mA, and Thorlabs M850L3, 850nm, 900 mW, 1200 mA. Each LEDs is driven using Thorlabs LEDD1B - T-Cube LED Driver, 1200 mA Max Drive Current. These LEDs needed to be coaligned on an axis and imaged on to the DMD chip for spatial modulation. The optical configuration for this purpose is based on Thorlabs's tutorial on collimating multi-LED sources [27]. On Figure 2.3, LEDs from left to right are 660, 730, and 850nm. On the cage system, light path is aligned from left to right cube via Thorlabs M24H00 Hot Mirror and Thorlabs FEL0800 Long-pass filter at 800nm, respectively. The area of the LED outputs in the case of collimation using an aspheric condenser lens becomes larger than the area of the DMD chip, Therefore, the biconvex lens is mounted on the output of the right

10

most cube and positions of aspheric condenser lenses where adjusted to image the LED chip with a slight defocus onto the DMD chip.
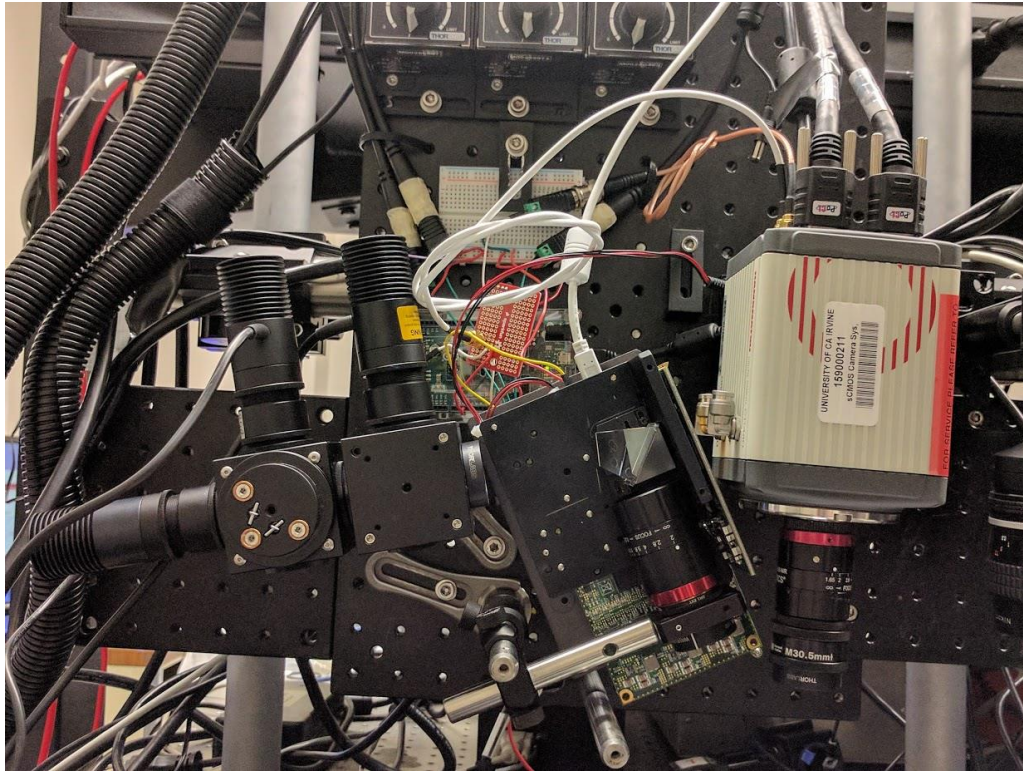
Figure 2.3 High speed SFDI Instrument (Version 2)

2.3   Results

The high speed SFDI platform can resolve heart rates of the animal up to 7 and 8.5 Hz for the Version 1 and Version 2 instruments. Figure 2.4 shows averaged reflectance at 656 nm of a ROI in the middle of the sample over the course of the experiment. Pulsatile information is visible from the time-domain data before the cardiac arrest as the heart of the animal is still beating. By taking FFT over a minute interval in this region, heart rate of the animal can be extracted. After the cardiac arrest where the animal enters asphyxia the pulsatile components are fully diminished from reflectance data.
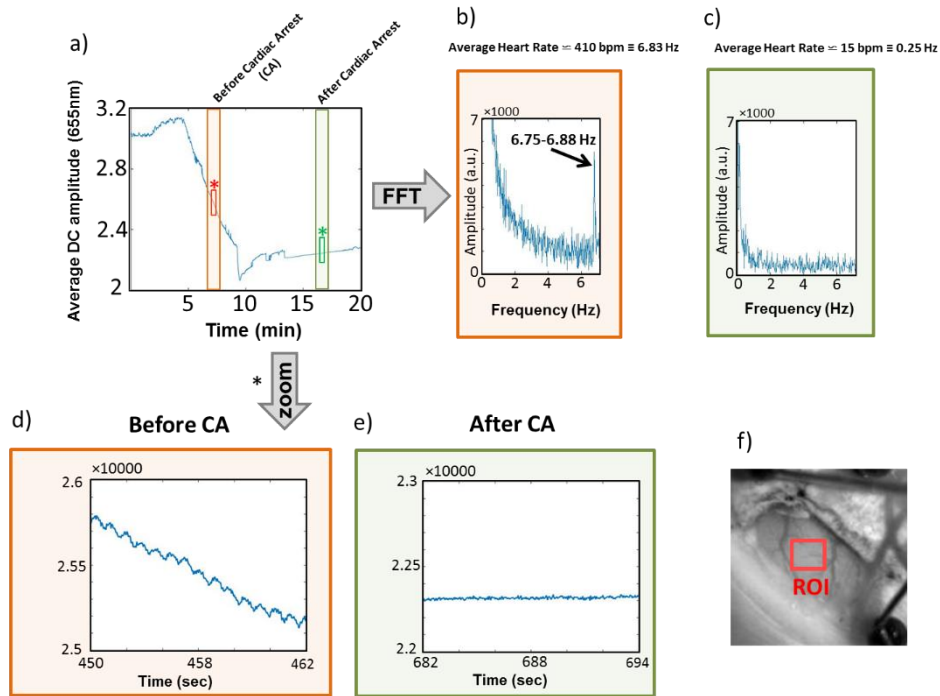
Figure 2.4 Extraction of heart rate using high speed SFDI instrument before and after the cardiac arrest

Figure 2.5 (a) shows maps of percentage changes (relative to baseline) in tissue deoxygenated hemoglobin concentration (ctHb) in the brain of a representative rat during asphyxia-induced ischemia and cardiac arrest, post-CPR reperfusion, and extraction of oxygen during resumption of cerebral electrical activity. During asphyxia, the blood supply to the brain is cut off, so ctHb increases sharply due to cerebral metabolism of the remaining oxygen. During post-CPR reperfusion, the brain receives a renewed blood supply, and ctHb decreases significantly because the brain is not yet metabolizing oxygen during this period. During the oxygen extraction phase leading up to resumption of cerebral electrical activity, the brain begins to metabolize oxygen so ctHb increases notably. Figure 2.5 (b) shows percentage changes relative to baseline in tissue deoxyhemoglobin concentration (ctHb, blue), tissue oxyhemoglobin concentration (ctHbO$_2$, red), tissue oxygen saturation (StO$_2$, purple), and tissue-reduced scattering coefficient (μ'_s) at 655 nm (green), over the ROI (dashed white box) shown in Figure 2.5 (a). Error bars represent the standard deviation over the ROI. The rapid SFDI system provides separate characterization of tissue

absorption and scattering with high temporal resolution over the course of the entire experiment. Inflection points in the scattering time-course coincide with CA-related cerebral ischemia, initial reperfusion of the brain following completion of CPR. Curves are shown relative to values just prior to the onset of asphyxia (t~4.5 to 4.8, rather than t=0) to highlight changes relative to "baseline" levels defined at the end of the anesthesia washout period. Figure 2.5 is derived from the publication [24].
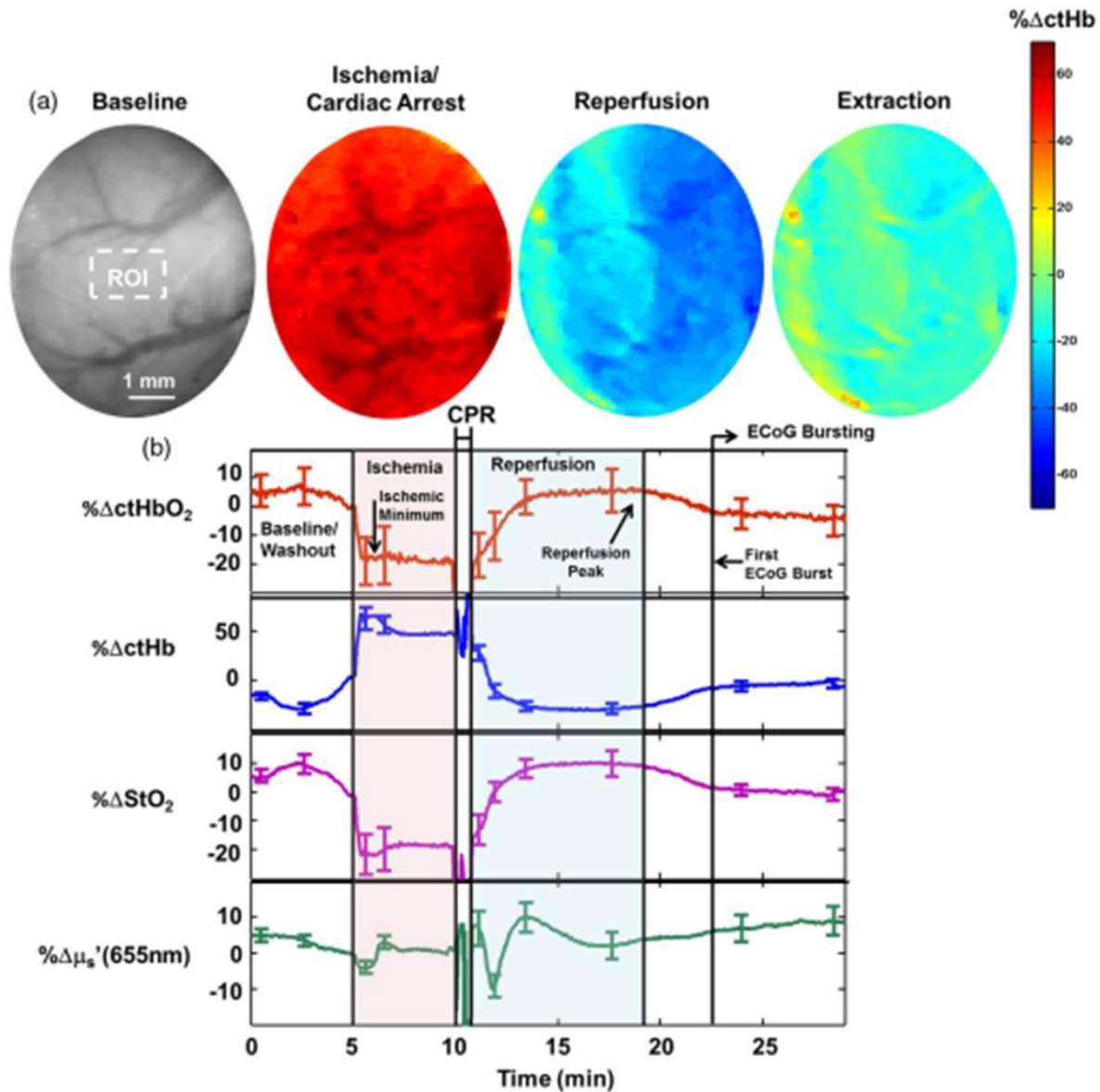
Figure 2.5 Plots of changes in oxyhemoglobin concentration ($\Delta ctHbO_2$), deoxyhemoglobin ($\Delta ctHb$), oxygen saturation (ΔStO_2), and reduced scattering at 655nm ($\%\Delta\mu'_s$) over multiple steps of the experiment: Baseline/Washout, Ischemia, CPR, Reperfusion, ECoG Bursting. ROI is chosen at the capillary bed shown in (a). Maps of changes in $\Delta ctHb$ is also shown in (a) at different phases of the experiment.

2.4   Discussion and Conclusion

Interpretation of spatiotemporal changes in oxygenation and scattering over the cardiac arrest and resuscitation experiment can be found in [24]. In conclusion, we developed a fast SFDI instrument has shown to be a reliable optical imaging platform to produce repeatable and reproducible

14

oxygenation measurement of a small animal's cerebral tissue at fine temporal resolution. The choice of light engine, spatial frequencies, and configuration on the high speed sCMOS camera were compatible with field of view, orientation of the animal, and absorption level of the sample. Long operating working distance of the instrument provided enough space for the intervening physician, Dr. Yama Akbari, to perform manual chest compression during the CPR part of the experiment and had no interference with the ECoG probes mounted on the cortex of the animal. The optomechanical design of the instrument allowed it to be transported to the animal operation room on weekly basis. The instrument has been used in more than 40 imaging sessions over a three-year period. Further studies can investigate correlations between data from pressure transducer mounted on peripherical arteries and cerebral total hemoglobin and blood flow from SFDI/LSI measurement using models of compressible fluid dynamics [28-30]. Long term monitoring of hemodynamics can neurological outcome is another future direction which is done via bio-compatible chronic imaging window on the skull [31, 32].

Chapter 3

3.   Hyperspectral Spatial Frequency Domain Imaging (hs-SFDI)

This chapter is derived from the publications [33, 34]. We introduce a method for quantitative

hyperspectral imaging (HSI) in the spatial frequency domain (hs-SFDI) to quantitatively image

tissue optical properties, absorption (μ_a) and reduced scattering (μ'_s) coefficients, over a broad

spectral range. The instrument utilizes principles of spatial scanning of the spectrally dispersed

output of a supercontinuum laser projected onto a digital micromirror device (DMD) for sinusoidal

pattern projection. An sCMOS camera is used for imaging and hs-SFDI performance is validated

using tissue-simulating phantoms, spectrophotometer measurements, and Mie theory analytical

models over a range of (μ_a) and (μ'_s) values. Quantitative hs-SFDI images were obtained from an

ex-vivo beef sample in order to spatially resolve concentrations of oxy- deoxy- and met-

hemoglobin as well as water and fat fractions. Our results demonstrate that hs-SFDI can

quantitatively image tissue optical properties with 1000 spectral bins in the 580-950 nm range over

a wide, scalable Field-of-View (FOV). With an average of accuracy of 6.7% in μ_a and 20.4% in

μ'_s compared to spectrophotometer results and Mie theory, respectively, hs-SFDI offers a

promising approach for quantitative hyperspectral tissue optical imaging.

3.1   Introduction

Biomedical hyperspectral imaging (HSI) combines high resolution spectral and spatial content in

order to characterize tissue structure and composition.   Because HSI typically employs hundreds

or thousands of optical wavelengths, multiple endogenous and exogenous tissue components with

unique spectral signatures can be resolved.   Various HSI technical approaches have been

developed for biomedical applications; most based on designs that generate reflectance and/or

fluorescence maps over a continuous spectral bandwidth [35-37].   Hyperspectral content can be

used in conjunction with computational models of light transport and various statistical methods, such as principal component analysis, to calculate optical and physiological properties in each pixel [38-40]. However, these methods generally require assumptions or approximations about certain tissue features such as scattering properties and water concentration [41, 42].

Quantitative, independent mapping of tissue absorption and scattering parameters, μ_a and μ'_s, respectively, for each wavelength and pixel is a significant technical challenge. Changes in each of these parameters have been well-documented to occur with variations in tissue molecular composition and structure, both for static tissue composition and for dynamic processes. In addition, quantitatively characterizing the extent of light-tissue interactions over a broad spectral range has been shown to be important in accurately recovering the spatial distribution and spectral features of both endogenous and exogenous tissue fluorophores [43, 44].

Spatial Frequency Domain Imaging (SFDI) is a wide-field non-contact model-based technique that quantitatively separates the contribution of absorption from scattering on a pixel-by-pixel basis by calculating the modulation transfer function of structured light projected onto tissue [14]. SFDI has been used extensively to characterize tissue optical and physiological properties and visualize quantitative maps of tissue oxy/deoxyhemoglobin concentrations both in-vivo and ex-vivo [17, 19, 45]. Hyperspectral SFDI has been developed using a single snapshot imager to characterize mouse brain [21] and has been combined with a hyperspectral line-scan camera to track brain tumor drug delivery in a rat model [22]. Konecky et. al. [46] utilized an Image Mapping Spectrometer (IMS) to simultaneously extract a hyperspectral cube with 38 wavelength bands from 484-652 nm at 5 Hz. This technique was applied to a rat model of whisker stimulation to track hemodynamic changes in somatosensory cortex. The hyperspectral data was then fed to a Diffuse Optical

Tomography (DOT) reconstruction algorithm to quantify hemodynamic changes in three spatial dimensions. SFDI was not employed in this work and tomographic reconstructions were constrained to measure absorption changes only.

With the development of real-time SFDI methods using square waves and fixed pattern projection combined with novel image demodulation strategies [25, 47, 48], spatial frequency modulation no longer imposes an imaging speed/informatics bottleneck. As a result, new SFDI strategies for increasing spectral content have been introduced using temporally encoded light sources [49] and single pixel compressive sensing [50], typically by employing a limited number of discrete lasers or LEDs. In this work we seek to significantly expand spectral content using a single supercontinuum laser in order to obtain broadband images distributed into 1000 spectral bins from 580-950 nm over a 4 cm×6 cm Field-of-View (FOV). Wavelength-tunability is achieved using dispersive optics and a scannable slit, while a spatial light modulator (SLM) is employed in pulse width modulation mode for conventional 3-phase sinusoidal projection. Images are formed using a high-speed s-CMOS camera that sequentially captures one spatial slice (x, y) of a spectral data cube while continuously sweeping through all wavelengths (λ). Other approaches for supercontinuum spectral selection have been introduced previously using both temporal encoding of spectral bins [51] and spatial filtering [52]. We assessed hs-SFDI performance by measuring tissue phantoms over a range of optical absorption and reduced scattering values and comparing results with Mie theory models and spectrophotometer data. Our results show that hs-SFDI can be a quantitative imaging system to extract tissue scattering properties and spectral fingerprints of multiple chromophores including oxy- deoxy- and met- hemoglobin as well as water and fat. These

parameters are clinically useful and can be incorporated in applications such as burn wound and diabetic foot ulcer assessments [53-55].

3.2 Materials and Methods

3.2.1 Hyperspectral SFDI Instrument

Our operating supercontinuum source (SC 400-2, Fianium, UK) is based on a 5-picoseconds diode pumped Yb fiber laser at 1064 nm. Once spectrally broadened, it generates continuous spectral output approximately in the 400-2100 nm range with the maximum total power of 2 Watts. Bandpass filtering of the broadband laser source was achieved by utilizing a folded prism Martinez compressor design. A prism (PS858, Thorlabs, Newton, New Jersey) spatially disperses the illumination beam on a plossl lens. The plossl brings the illumination beam to a line focus onto a slit (VA100, Thorlabs, Newton, New Jersey) which is mounted on a linear stage (TLS13E, Zaber Technologies Inc, Vancouver, BC) and in front of a mirror. This configuration allows for tuning the spectral bandwidth and central wavelength of the broadband laser input. The plossl lens is moved down from the optic axis to steer the beam down so that it can be easily picked off with a D-mirror after the second pass through the prism. The wavelength-tuned beam is then expanded. To reduce spatial heterogeneity, the beam is transmitted through a high grit diffuser (DG100-600-B, Thorlabs, Newton, New Jersey) prior to the Digital Micro Mirror Device (DMD) (CEL5500, Digital Light Innovation, Austin, Texas). The DMD produces 8-bit gray scale sinusoidal patterns through time sharing Pulse Width Modulation (PWM) method. The spatially modulated light is finally imaged onto a sample and diffuse reflectance light is captured via a high speed scientific Complementary Metal Oxide Semiconductor (sCMOS) camera (ORCA-Flash 4.0 V2, Hamamatsu Photonics K.K., Japan). A schematic of the instrument is shown in Figure 3.1.
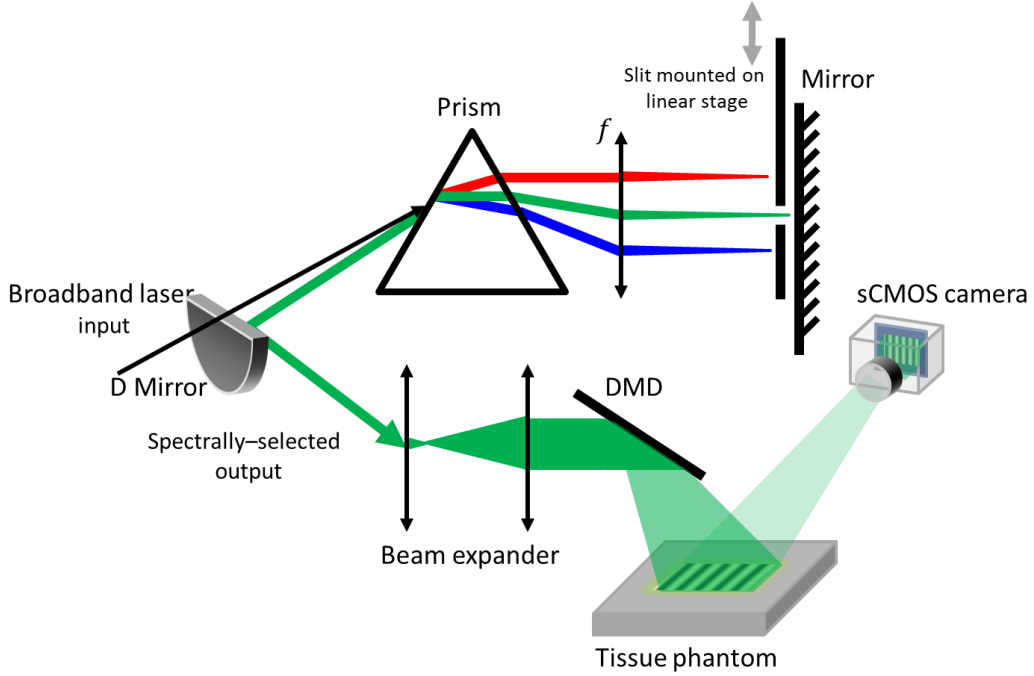
Figure 3.1 Schematic of the hs-SFDI instrument.

To increase Signal to Noise Ratio (SNR), pixels were binned by a factor of 4 which gave the image resolution of 512×512 pixels over a 4 cm×6 cm FOV. The camera captures images using the internal running mode and its exposure time, 50 ms, is adjusted to pattern refresh rate of the DMD. Each scan of the moving slit provided 1000 images.

3.2.2 SFDI Processing

In this paper, we used a single spatial frequency ($f_x = 0.1$ mm^{-1}) sinusoidal pattern at three $2\pi/3$ rad shifted phases which were then inserted to the following SFDI demodulation Equation 3-1

:

Equation 3-1

$$AC(x, y) = \frac{2^{1/2}}{3} \{[I_{0°}(x, y) - I_{120°}(x, y)]^2 + [I_{120°}(x, y) - I_{240°}(x, y)]^2 + [I_{240°}(x, y) - I_{0°}(x, y)]^2\}^{1/2}(1)$$

20

Where AC(x, y) is demodulated reflectance at pixel (x, y) and I_θ (x, y) is intensity of phase θ at pixel (x, y). The DC demodulated reflectance was acquired by averaging over phase shifted single frequency images, Equation 3-2:

$$DC(x,y) = \frac{1}{3}(I_{0°}(x,y) + I_{120°}(x,y) + I_{240°}(x,y))$$

Equation 3-2

The following procedure is then performed to calculate optical properties of a sample:

1. Demodulated AC and DC images are calculated for a calibration phantom using the hs-SFDI instrument.

2. Optical properties of the calibration phantom can either be calculated using an integrating sphere setup based on Inverse Adding Doubling (IAD) technique or through broadband multi source-detector separation measurement using Frequency-Domain Photon Migration (FDPM) technique [56].

3. A forward Monte Carlo (MC) simulation of radiative transport in turbid media is performed using previously acquired optical properties and true diffuse reflectance values are calculated for both AC and DC components.

4. Sample's AC and DC components are divided by their calibration images and multiplied by MC-derived diffuse reflectance values to correct for instrument response and to calculate absolute diffuse reflectance values of the sample.

5. AC and DC calibrated reflectance values are finally inserted to an inverse MC solver to extract a unique pair of optical properties (absorption and reduced scattering).

3.2.3   Spectral characterization

Figure 3.2 shows a plot of slit location as a function of nominal/central bandwidth. Intensity profile across the spectrum is also shown with a peak intensity at 740 nm. We chose 1000 slit locations corresponding to 1000 spectral bins in the 580-950 nm region and measured output

spectra using a spectrometer (Blue Wave, Stellar Net Inc., Tampa, Florida). Slit width is set to 200µm. Mean and Standard Deviation (SD) of Full Width at Half Maximum (FWHM) was calculated to be 17.25 nm and 5.69 nm respectively. As it was expected, lower $dn/d\lambda$ (n: refractive index of prism material, λ: Wavelength) at longer wavelengths on the dispersive prism led to increase in spectral bandwidth, reaching 26.42 nm for the 950 nm spectral bin.
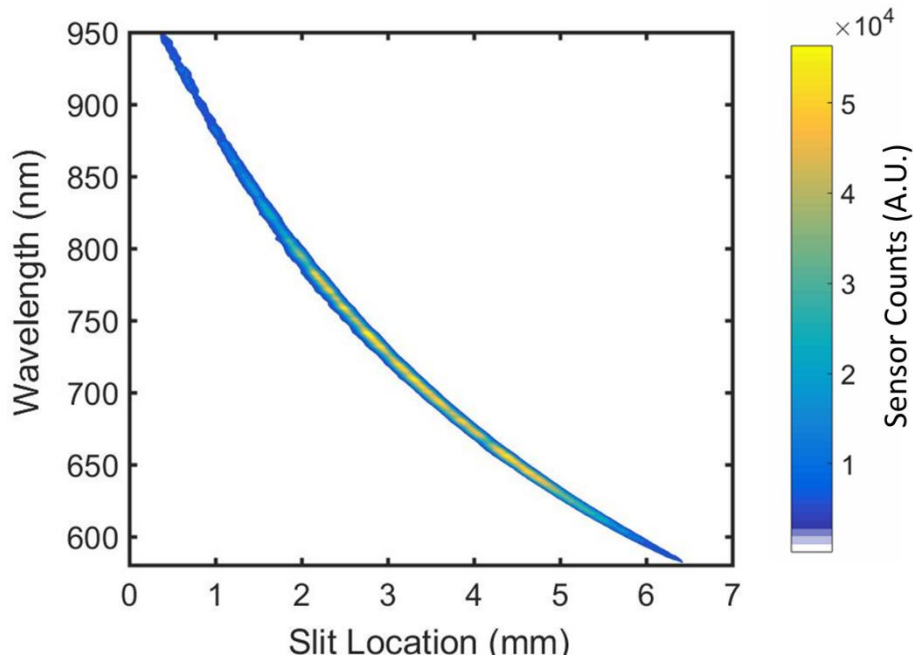
Figure 3.2 Slit location versus nominal wavelength

Most of the spectral features of main chromophores (Oxy/deoxy/methemoglobin, fat, and water) in the first optical window (600-1000 nm) are, however, broader than achieved bandwidth using the hs-SFDI instrument. That said, to accurately separate and quantify chromophores specially for those with distinct features at wavelengths longer than 900 nm (fat and water), robust fitting and peak separation approaches may be considered [43].

3.3 Results

3.3.1 Multi-concentration liquid phantom

To experimentally validate the performance of the broadband hyperspectral imager, we performed a series of controlled tissue phantom measurements to demonstrate that the instrument can quantify absorption and reduced scattering in a wide spectral range. We built a solid tissue phantom from silicone as base material, India ink as absorbing agent, and Titaniun(IV) Oxide (TiO2) (Sigma Aldrich, St. Louis, Missouri) as scattering agent. More details on the phantom making procedure can be found in [57]. We then inserted 12.5 mm diameter cylindrical molds in the base phantom. Once the base phantom cured, we removed the cylindrical molds and poured liquid solutions in the resulted "wells". A schematic of the tissue phantom is shown in Figure 3.3.
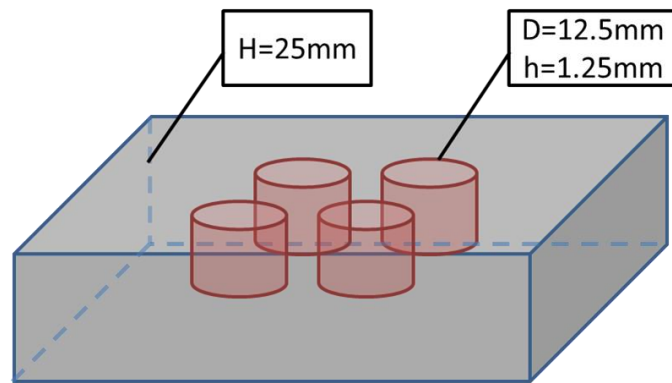
Figure 3.3 A schematic of the multi-well tissue phantom with silicone base material.

We made distilled water-based solutions of Naphthol Green B at multiple concentrations (0.25, 0.03125, 0.0375, 0.04275 and 0.05 g/L). We then measured each solution with a custom-built spectrophotometer in the transmission mode to calculate its absorption coefficient from 580 to 950 nm. We finally made turbid versions of the same solutions by adding Intralipid (Fresenius Kabi, Uppsala, Sweden) to them. We added 1 mL of 20% Intralipid to 19 mL of each solution, poured them into the wells of the phantom depicted in Figure 3.3, and measured the sample with the

hyperspectral SFDI instrument. The measurement is performed at 1000 spectral bins in the 580-950 nm region, however, we selected 208 linearly spaced bins for the sake of simplicity.

Figure 3.4 shows absorption coefficient values of 5 Naphthol Green B solutions extracted using the hyperspectral SFDI instrument and the spectrophotometer. The μ_a of these solutions ranged from 0.015 to 0.087 mm^{-1} while μ_s' ranged from 0.75 to 1.8 mm^{-1}. Figure 3.5 shows extracted reduced scattering plots for the five solutions. The optical properties were determined by averaging over a 6 mm×6 mm Region of Interest (ROI) over the center of each well. Mean spatial SDs in absorption and reduced scattering maps of these ROIs are 0.0019 mm^{-1} and 0.0488 mm^{-1} which gives coefficients of variation of %3.949 and %3.614, respectively. It is expected to extract similar μ_s for these solutions since the dominant scattering contribution originates from their similar Intralipid concentrations. While there is variation in Intralipid batches [58], we show that the hs-SFDI-fitted μ_s values are within 20.4% (SD 6.1%) of 1% Intralipid μ_s values predicted by Mie theory [59].
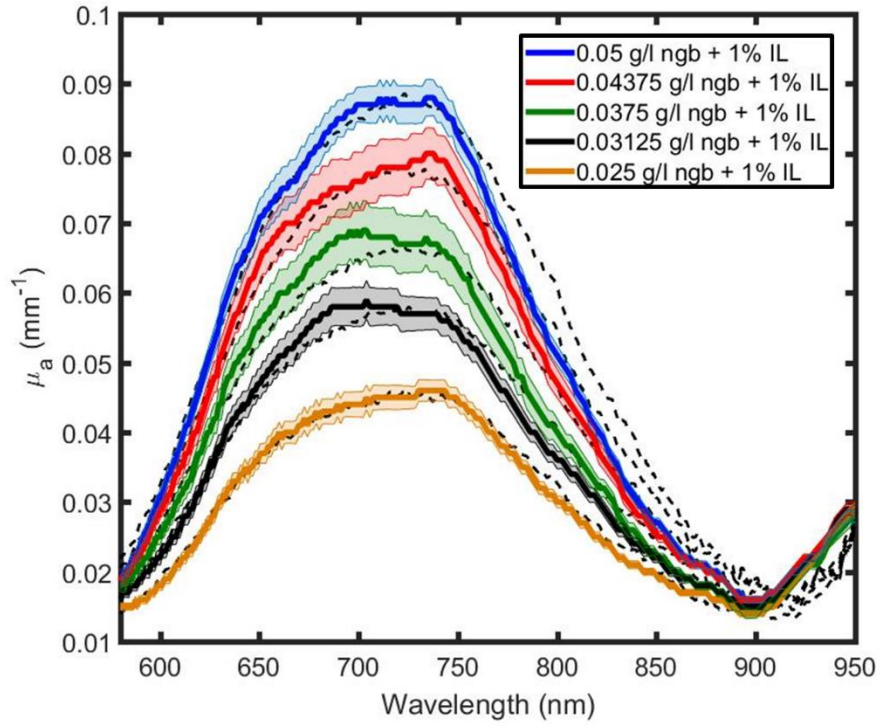
Figure 3.4 Plot of bulk μ_a spectra for five concentrations of Naphthol Green B. Colored lines are from the hs-SFDI instrument and black dotted lines are spectrophotometer measurements.
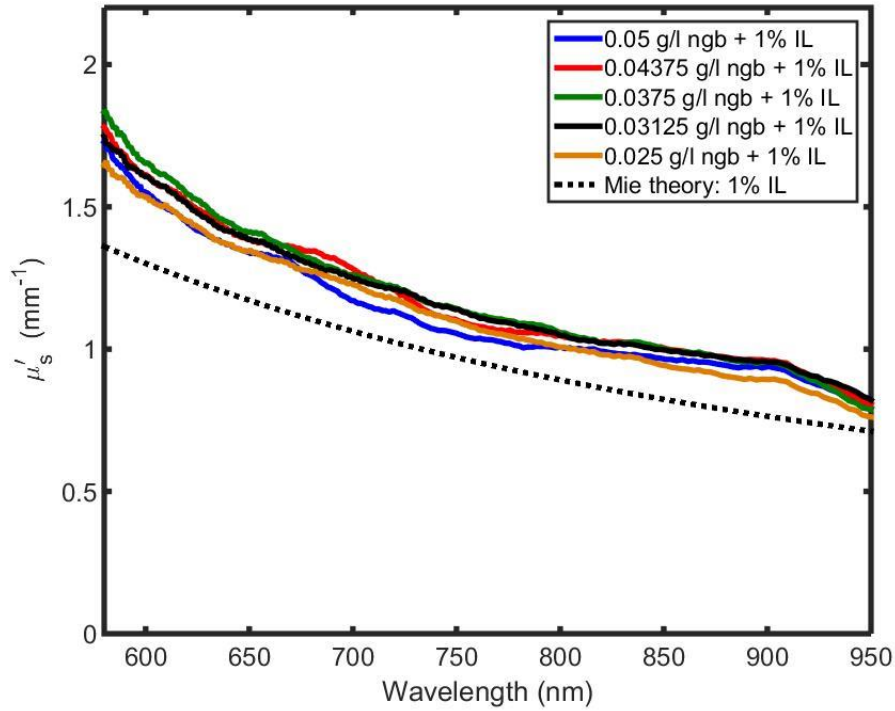
Figure 3.5 Plot of bulk μ'$_s$ spectra for five concentrations of Naphthol Green B solutions with 1% Intralipid concentration. Colored lines are from the hs-SFDI instrument and black dotted line is analytical μ'$_s$ spectra derived from the Mie theory. Standard deviations are not shown to avoid clutter.

The average difference between recovered μ$_a$ values using the hs-SFDI instrument and spectrophotometer was 6.7% (SD 6.8%).

Figure 3.6 (a) shows fit intervals for the expected μ_a values, spectrophotometer results, and those obtained using the hs-SFDI instrument for all five solutions at 208 wavelengths. Figure 3.6(b) shows Bland-Altman plots [60] of recovered optical absorption for the same data set. 94% of hs-SFDI measurements were within 1.96×SD of the mean difference indicating a close agreement between the two approaches. The data points with errors larger than 1.96×SD are more significant for absorption coefficients less than 0.02 mm^{-1}, specially for wavelengths longer than 750 nm where bandwidth of spectral bins become larger due to lower $dn/d\lambda$ imposed by the dispersive prism in the optical configuration. However, other factors such as partial volume effect

from the surrounding medium at lower absorption values and low SNR at higher wavelengths could also contribute to this effect.

(a)   (b)
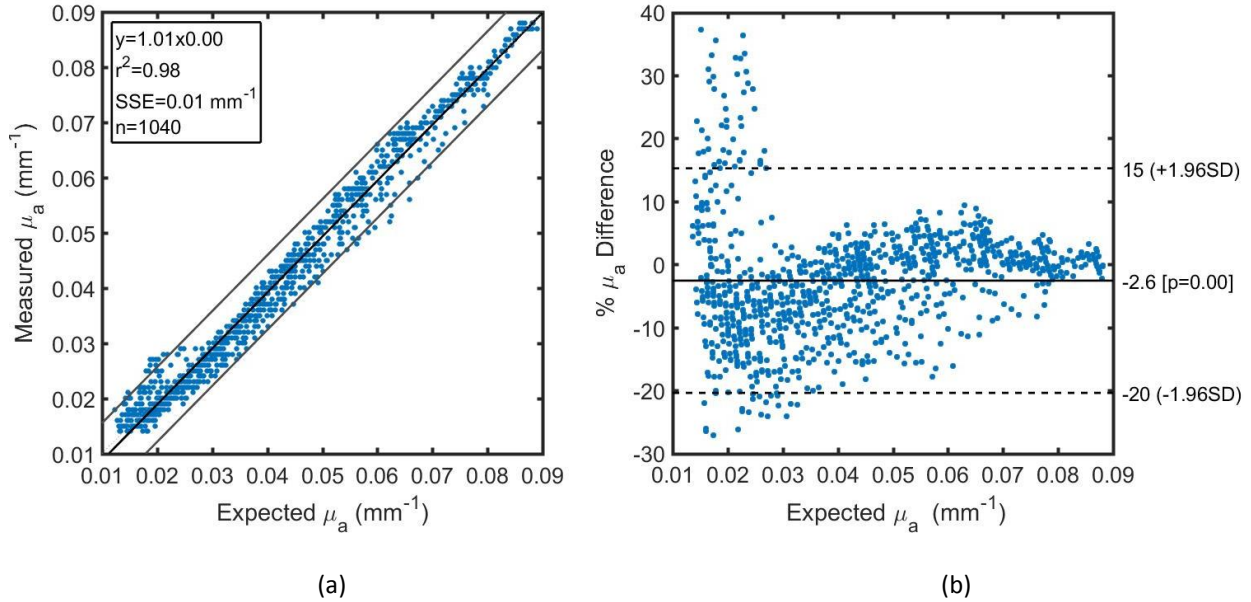
Figure 3.6 (a) Fit intervals. (b) Bland-Altman plots of mean and percent difference of extracted μ_a from the spectrophotometer (Expected μ_a) and hs-SFDI (Measured μ_a)

3.3.2 Multi-dye phantom

In this section, we made solutions of four compounds with distinct spectral features: blue food dye (Ateco, Glen Cove, New York), extra virgin olive oil, Naphthol Green B (Sigma Aldrich, St. Louis, Missouri), and FHI96716 dye (Fabricolor Holding Int'l, Paterson, New Jersey) with absorption peaks at 636, 675/930, 730, and 910 nm, respectively. We then made turbid version of these solutions by adding 20% Intralipid to them so that the resulted concentrations of Intralipid will become 1% except for the olive oil where we diluted known concentration of TiO_2. The four solutions where then poured in wells of a silicone phantom built using the same method described in Section 3.1. We measured the sample using the proposed hs-SFDI instrument and extracted μ_a and μ_s' for 1000 spectral bins in the 580-950 nm range. Figure 3.7 shows absorption spectra for the four solutions. The optical properties were determined by averaging over a 6 mm×6 mm region

27

over the center of each well. The spectral shape of these solutions agrees with the expected absorption spectra trend reported for each of them. There is however some cross-talk between the sample and the calibration phantom in the 890-910 nm region where we believe arises from the silicone absorption peak in the calibration phantom. μ_a maps of the multi-well phantom are shown in Figure 3.8 at 6 distinct wavelengths. While averaging over the center of each well gives a bulk optical property value, there are partial volume effects next to edges as large pathlengths allow photons from the solid medium to enter each well, thus distorting localization of optical properties.
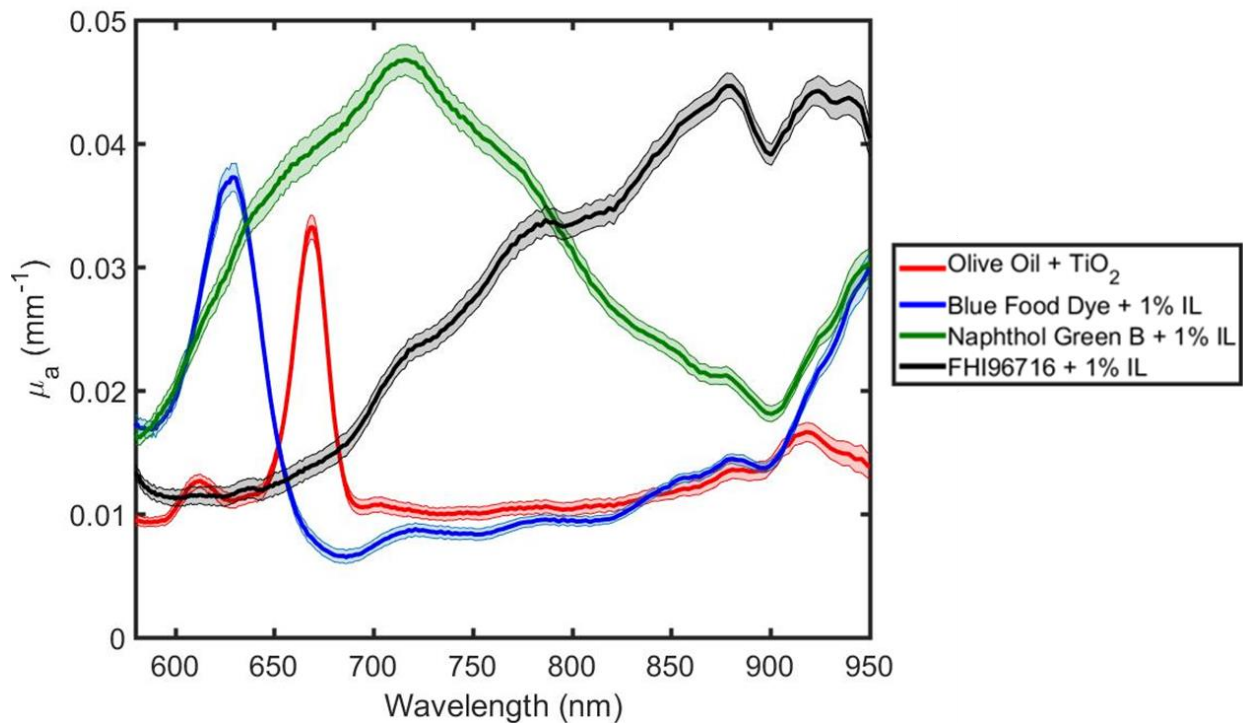
Figure 3.7 Plot of bulk μ_a spectra for four solutions: three water-soluble dyes with 1% IL concentration. Olive oil is mixed with known concentration of TiO2.

Figure 3.9 shows reduced scattering spectra for 4 solutions. As it was expected, the 3 water soluble dyes with 1% Intralipid concentration present values close to each other and theoretical reduced scattering spectra from Mie theory. There are, however, increased deviations in reduced scattering values compared to 3.3.1. This could be related to photons propagating through multiple mediums

28

in the phantom with different refractive indexes and optical properties or minor spatial variations in the calibrated reflectance.
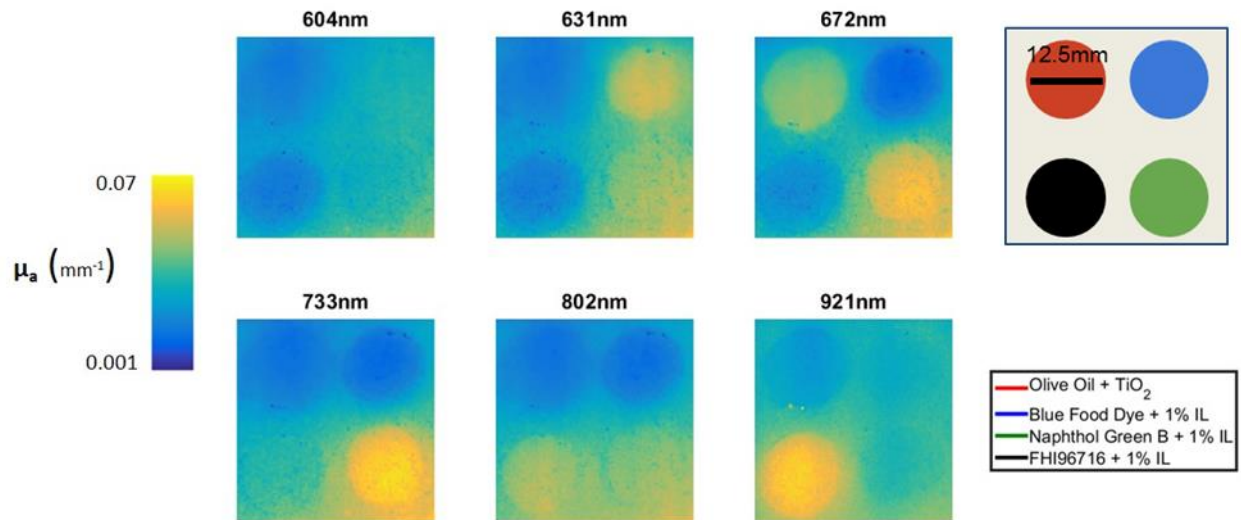
Figure 3.8 μ_a maps of multi-well phantom at 6 wavelengths.
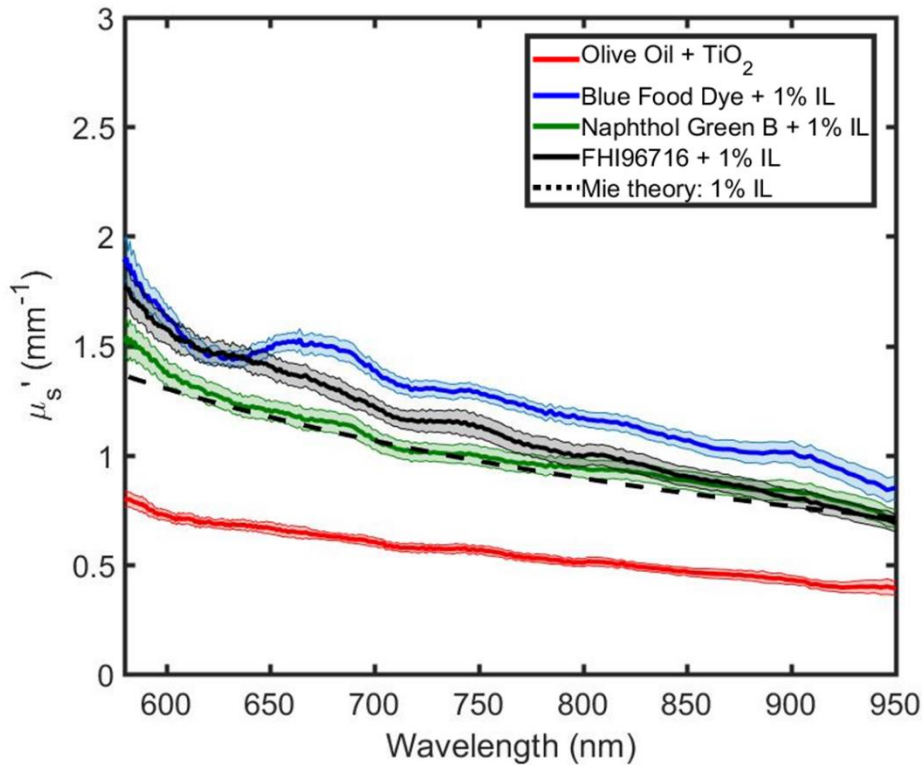
Figure 3.9 Plot of bulk μ'_s spectra for four solutions: three water-soluble dyes with 1% IL concentration. Olive oil is mixed with known concentration of TiO2. Colored lines are from the hs-SFDI instrument and black dotted line is analytical μ'_s spectra derived from the Mie theory.

3.3.3 Dye Mixing

We performed a phantom measurement where we mixed same volumes of two near-infrared absorbing solutions, Naphthol Green B and Nickel(II) Phthalocyanine. We then measured the mixture together with pure solutions of two species using the hs-SFDI instrument. All water-based solutions are mixed with Intralipid to result in 1% concentration. Figure 3.10 shows a plot of absorption spectra for pure solutions and the mixture. Since same volumes of the pure solutions where used to form the mixture (50-50 Mix + 1% IL), absorption spectra of the mixture would theoretically be equal to average of absorption spectra of its components. These averaged spectra are also depicted in Figure 3.10 as theoretical mixture spectra.
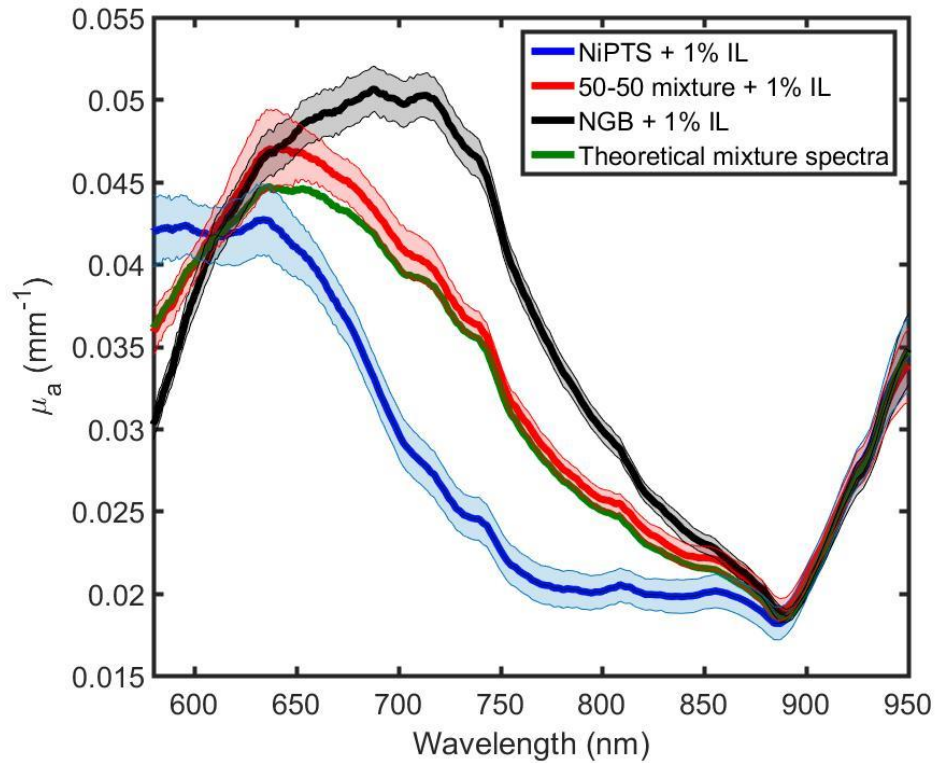
Figure 3.10 μ_a spectra of 1% IL solutions of pure Naphthol Green B, Nickel(II) Phthalocyanine, mixture of these two components, averaged values for pure Naphthol Green B and Nickel(II) Phthalocyanine

We then fitted the absorption spectra at every pixel to extinction coefficient spectra of Naphthol Green B and Nickel(II) Phthalocyanine to extract their concentration maps. Figure 3.11 shows concentration maps of these two components. At is was expected, concentration of both species in the mixture are approximately half of the value of their pure solutions. This experiment shows how the hs-SFDI instrument can be used to quantify concentration of known species in a controlled mixture. In tissue samples where there are multiple chromophores with overlapping absorption spectra, prior knowledge on dominant constituents and their absorption spectra is necessary to select spectral bins of the broad bandwidth and then quantify chromophore concentrations.
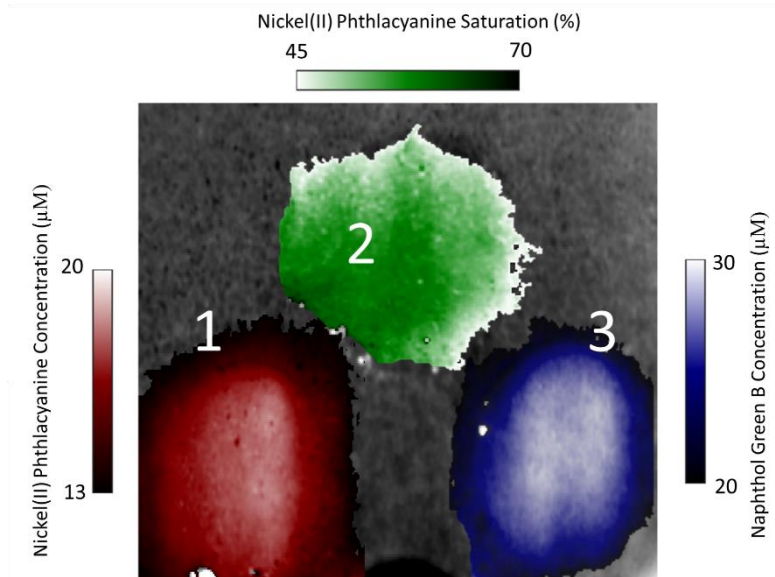
Figure 3.11 Concentration maps of Naphthol Green B (Blue colormap) and Nickel(II) Phthalocyanine (Red colormap) in micromolar (µM). Saturation of Nickel(II) Phthalocyanine (Green colormap) calculated by dividing its concentration by total concentrations of the mixture. Tagged samples are: 1. Pure Nickel(II) Phthalocyanine + 1% IL, 2. %50-%50 Mix + 1% IL, and 3. Pure Naphthol Green B + 1% IL.

3.3.4 Beef sample

In this section, we measured a low sirloin steak that consisted of fat and muscle spots using the hs-SFDI instrument. Figure 3.12 shows absorption and reduced scattering spectra for two 5 mm×5 mm ROIs located on the fatty and muscle part of the sample.
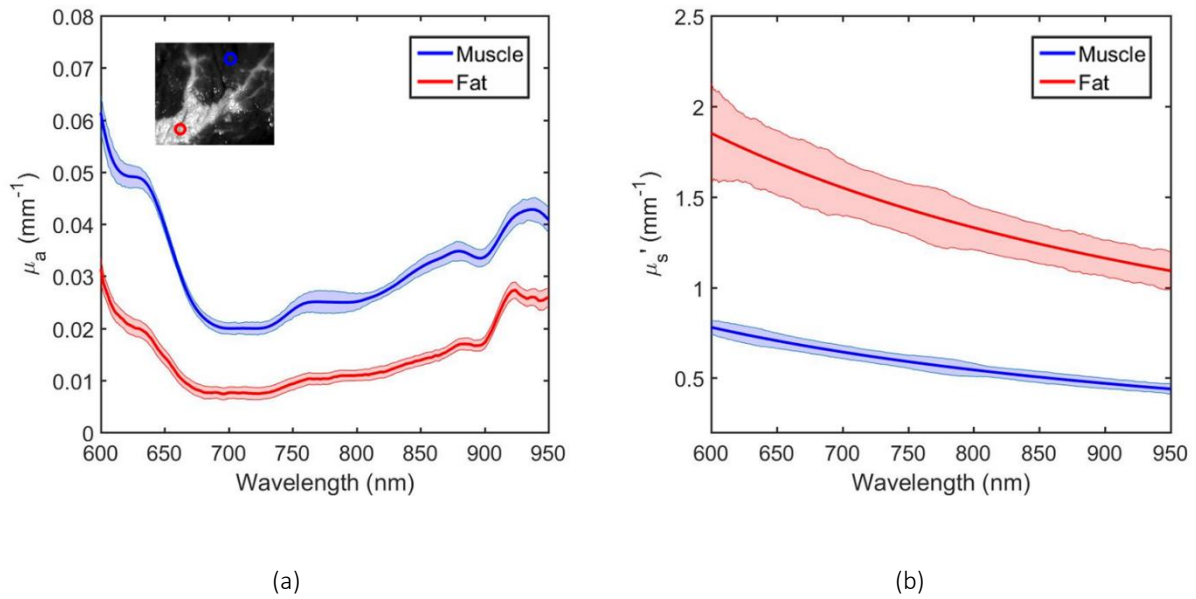
Figure 3.12 Plot of (a) bulk μ_a and (b) μ_s' spectra at two ROIs: Fat (red) and Muscle (blue)

The absorption spectra have local maximums, as shown in Figure 3.12(a), at 600 and 630 nm mostly due to deoxy/oxyhemoglobin and methemoglobin absorption, respectively. These peaks are noticeable for both ROIs due to partial volume effect in the sample and spatial heterogeneity in three dimensions. Increase in absorption values at 850 nm and longer wavelengths is seen in both fatty and muscle components. There is also a fat absorption peak at about 920nm. The overall trend and magnitude of absorption and reduced scattering spectra on the muscle part agrees with what reported in previous studies [61, 62]. On the reduced scattering spectra, Figure 3.12(b), the fatty part shows higher values than the muscle part. These values are comparable to previous reports in [63] as average(standard deviation) of A and b parameters for fatty tissue from 6 studies are 1.288(0.630) mm^{-1} and 0.672(0.242), respectively. The average(standard deviation) of A and b parameters of muscle/heart tissue from 4 studies are 0.531(0.224) mm^{-1} and 1.609(0.722), respectively.

Figure 3.13 shows absorption and reduced scattering maps at two wavelengths (600 and 950nm).

As it is shown in Figure 3.13(a), dominant contrast between the fat and muscle parts arises from oxy/deoxyhemoglobin absorption at 600 nm. Increase in fat and water absorption at 950 nm decreases spatial absorption contrast between the fat and muscle part, Figure 3.13(b).
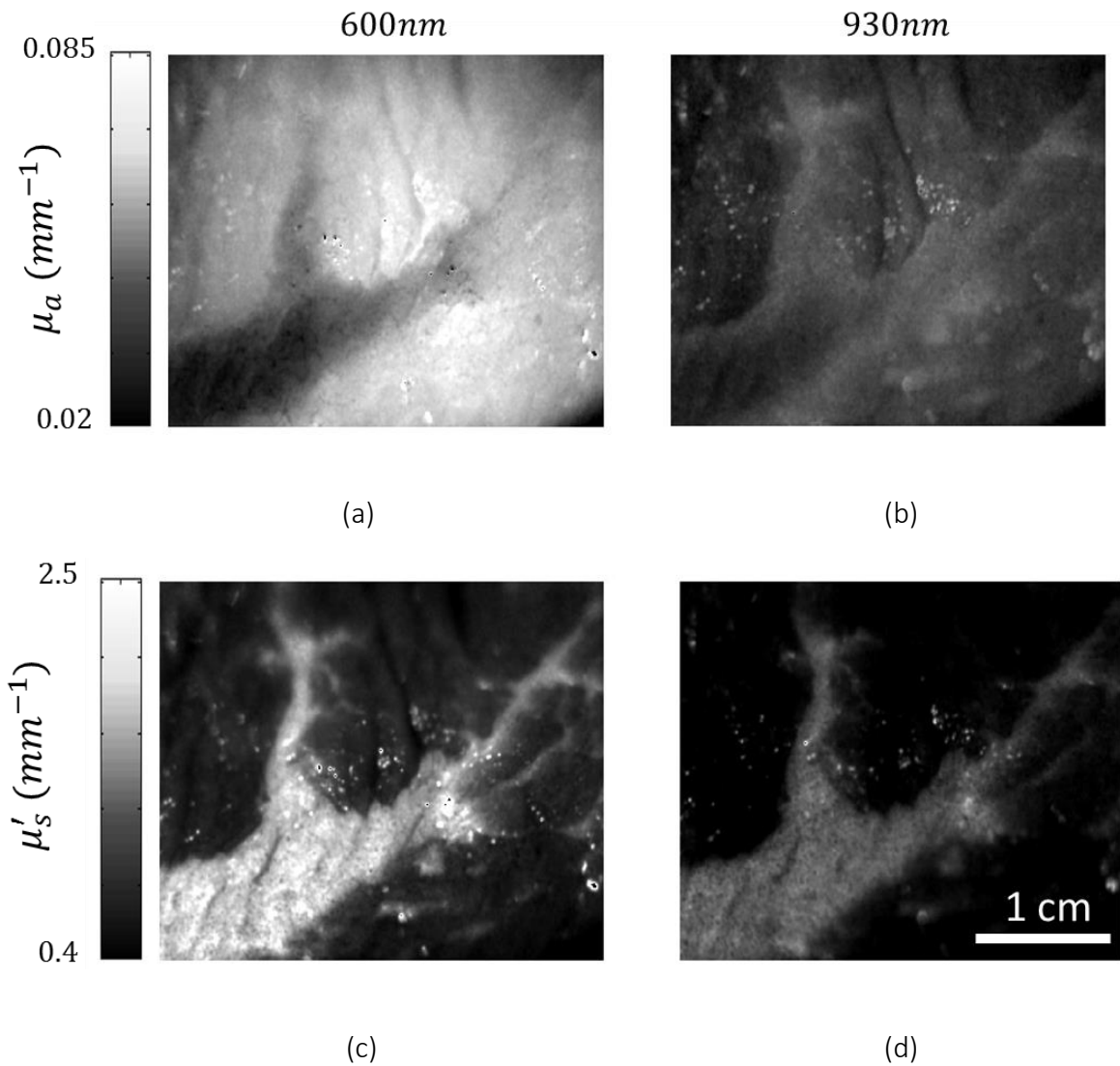
Figure 3.13 Absorption (μ_a) and reduced scattering (μ'_s) maps of the beef sample at 600 and 950 nm

We finally fitted the absorption spectra at two ROIs (fat and muscle part) to 5 chromophores: oxyhemoglobin (HbO₂), deoxyhemoglobin (Hb), methemoglobin (MHb), fat, and water using

Beer-Lambert law and Matlab (Mathworks Inc, Natick, Massachusetts) lsqlin function. Table 1 shows extracted values and standard deviations for these chromophores in 2 ROIs.

	Hb (µM)	HbO2 (µM)	MHb (µM)	Fat (Fraction)	Water (Fraction)
Fat ROI	0.10(0.08)	41.7(4.54)	4.0(0.05)	0.7503(0.04)	0.5211(0.06)
Muscle ROI	1.3(0.73)	92.3(8.19)	9.1(0.57)	0.4186(0.05)	0.5948(0.05)

Table 3-1 Chromophore concentration and fraction values for two ROIs (fat and muscle) in the beef sample. Standard deviation of values in each ROI are included in parentheses.

The extracted values match with expected higher hemoglobin concentrations and water fraction in the muscle part. Overlap of MHb with fat and water absorption peaks and large bandwidth of spectral bins in the 850-950nm region, decreases ability to fully decouple and resolve these chromophores, thus causing possible underestimation of MHb and overestimation of fat in the muscle part. We excluded spectral bins in the 580-600 nm region in chromophore fitting procedure due to low SNR imposed by hemoglobin absorption in the sample. In general, there are many issues including type of skeletal muscle, date of harvesting, packaging, and aging procedure that can cause variations in sample's constituents. Depth of interrogation also differs across the spectral bandwidth which can prevent sampling the same volume of tissue. Full control over these parameters are out of the scope of this study but may allow for more accurate estimation of tissue constituents.

3.3.5 Integration to single pixel camera and light labeling

While we mainly focused on a time-domain scanning technique and focal array sensor in the

previous section. The proposed hyperspectral projection unit can also be implemented to a frequency-domain technique where each spectral bin is temporally modulated at distinct frequency. Hyper-Spectral information is encoded in the illumination beam by temporal modulation, so-called Light Labeling (LiLa) [51]. LiLa works by uniquely modulating each spectral component with a temporal frequency. The light labeling can be thought of from a communication theory perspective, where each modulation frequency represents a channel and each channel contains spectral information. The channels can be multiplexed because they form an orthogonal basis. It is well known that sinusoids produce an orthogonal basis, which means each spectral component can be readily recovered by projecting the time signal onto a sinusoidal basis, that is, taking the Fourier transform of the time signal will recover the power spectrum. It was shown in [64] that LiLa can be used with a conventional 2D array detector, however, this method is very slow and requires hundreds of images to be taken to recover the spectral information. If, instead, a single element detector is used for detection the large bandwidth may be leveraged to rapidly acquire the spectral information while simultaneously obtaining the 2D information using a single pixel camera. An additional advantage of the single element detector is the broad range of detectors that may be used to capture spectral information outside of the visible band where traditional 2D detectors fall short in terms of SNR, pixel density, cost, and availability. We previously assessed the single pixel camera performance in the context of a multi-spectral SFDI instrument [50]. We showed agreement in optical property extraction using a conventional camera and the single pixel approach. Compressed Sensing (CS) technique was used to decrease total number of measurements required to reconstruct an image using the single pixel camera. In a single pixel hyperspectral SFDI instrument, LiLa is achieved through mounting a spinning disk reticle at the focal plane of the folded Martinez compressor. The mentioned modifications result

in the following instrument schematic, Figure 3.14:
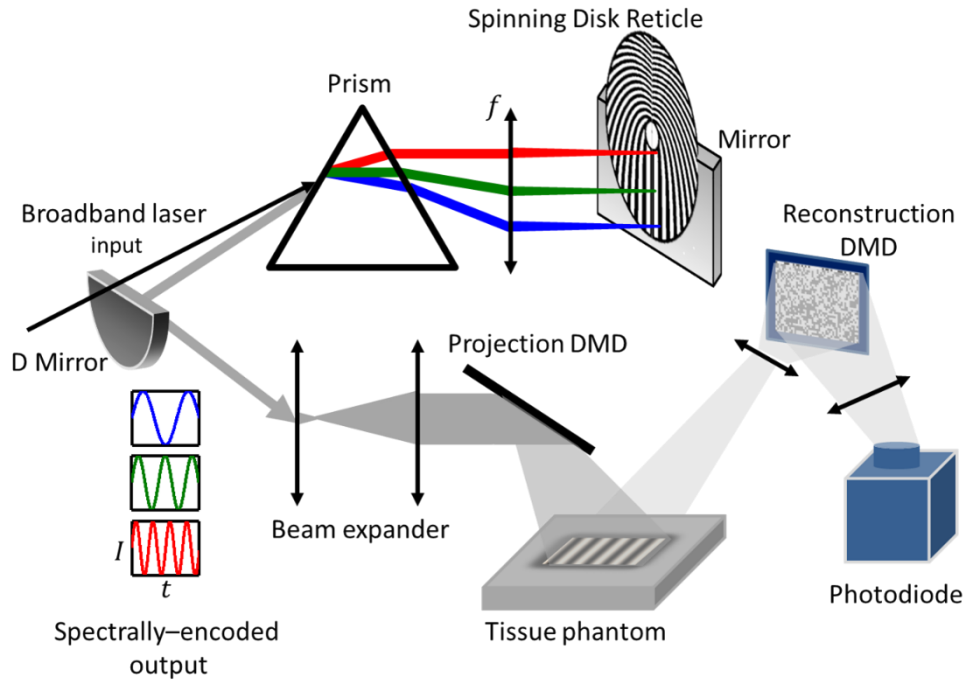
Figure 3.14 Schematic of the compressed single pixel H-SFDI instrument.

We performed preliminary tissue phantom measurement to reconstruct images using a single pixel camera with CS technique [65], and spectrally encoded supercontinuum output using LiLa. Figure 3.15 shows image reconstructions at 8 spectral bins with approximate bandwidth of 30 nm. One side of the silicone-based tissue phantom is made of naphthol green b as absorptive agent and TiO_2 as scattering agent. The other side is a Spectralon with theoretical 99% reflectance (Spectralon, Lab Sphere, North Sutton, New Hampshire). The reconstructed images were 64×64 in pixel resolution with compression ratio of 5. DC pattern is projected onto the sample in this measurement.
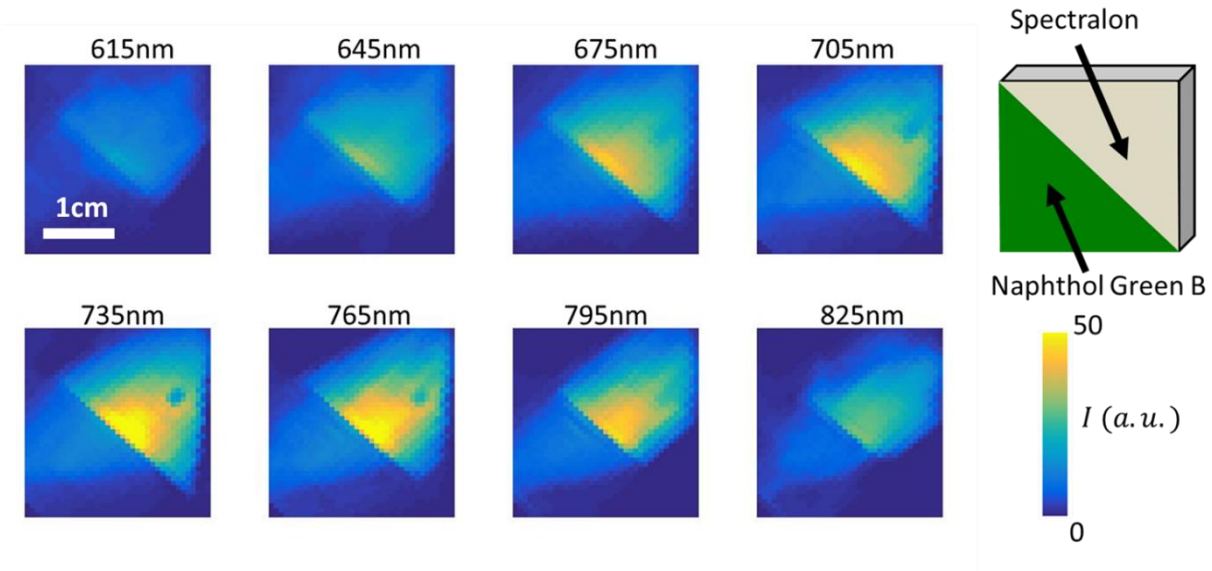
Figure 3.15 Reflectance maps at 8 spectral bins (Bandwidth=30nm) and schematic of phantom

At each spectral bin, we then chose an ROI on two sides of the phantom and calibrated the naphthol green b part via dividing its intensity by Spectralon intensity. We then corrected for the contribution of scattering properties using a Monte Carlo (MC) simulation of radiative transfer turbid medium and calculated absorption coefficients at multiple spectral bins. As it will be discussed in this section, we faced poor reconstruction quality at AC frames of SFDI workflow and therefore estimated scattering values from known $TiO2$ concentration. Figure 3.16 shows plot of our absorption spectra for the naphthol green b phantom. The extracted values follow absorption spectra trend of naphthol green b in silicone.
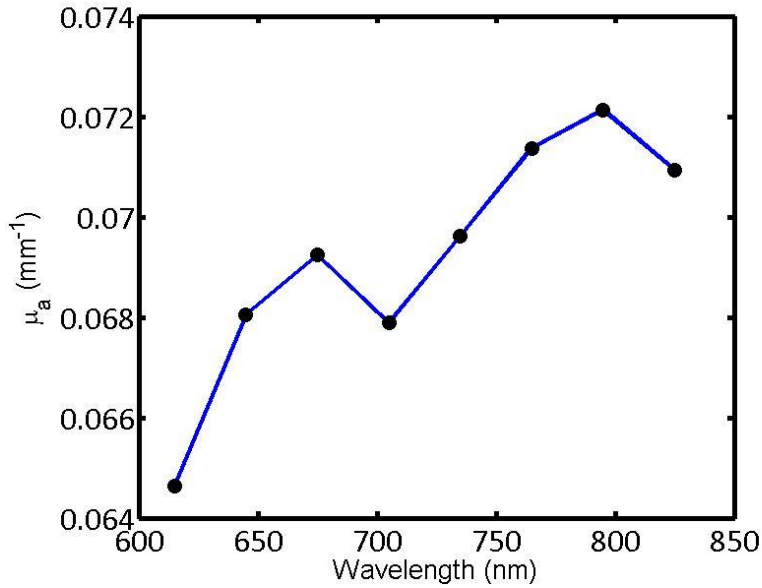
Figure 3.16 μ_a at 8 spectral bins acquired using the single pixel hyperspectral SFDI instrument

One of challenges with integrating the light-labeling H-SFDI instrument to our compressed single pixel camera was susceptibility of image reconstructions to subtle temporal/spectral oscillations in the supercontinuum source output. What considers to be sampling contrast from one random pattern on the single pixel camera to another random pattern can be about 8% difference in intensity depending on measurement phantom. A stack of these intensity values acquired from the photodiode of the camera are finally inserted to a CS algorithm for image reconstruction. However, we confronted 1-2% random source noise both spectrally and temporally which distorted CS reconstructions when it came to SFDI workflow, specifically reconstruction of AC frames. Further intensity calibration approaches in the frequency domain need to be applied to this instrument so that raw reflectance images provide enough Signal-to-Noise Ratio (SNR) for accurate optical property extractions.

3.4 Discussion

In this paper, we focused on validating the performance of the hs-SFDI instrument in a range of

optical properties over a wide spectrum. One of the challenges with the current wavelength-tuning configuration is acquisition speed. It takes about 150 seconds to acquire a hyperspectral cube at 3 AC phases since the slit scans a 6.3-mm line at the speed of 0.1209 mm/s which is equivalent to a total bandwidth of 370 nm. The scanning slit can technically move at maximum speed of 6.5 mm/s which enables it to cover the entire bandwidth in less than a second, thus 3 seconds in total for 3 phases. However, at our current large FOV (4 cm×6 cm), this requires extremely higher sinusoidal pattern refresh rate on the DMD and lower exposure time on the camera which are not applicable with the current components.

One solution to overcome refresh rate limitation of the DMD would to be switching to square waves from sinusoidal patterns. The 8-bit refresh rate on the current DMD is 60 Hz. This rate increases to 5 kHz for binary patterns. This approach has been utilized in a video-rate multi-spectral SFDI instrument to track hemodynamics in a preclinical rat model of cardiac arrest and resuscitation [24, 66]. Additionally, square pattern illumination can synthesize multiple spatial frequency components (fundamental and harmonic) to probe multiple depths [25]. In the case of homogeneous samples, using diffuse reflectance values at multiple spatial frequencies can also help minimizing μ_a and μ'_s fitting error [67]. The alternative solution would be single snapshot techniques which do not require three phase projections [47, 68]. However, these techniques require large number of cycles in the modulation pattern to mitigate ringing artifacts and may not be applicable to small field of views [47].

Choosing an optimized exposure time of the camera is mainly dependent on total light throughput, power distribution on both tails of the spectral bandwidth, and sensitivity of the camera sensor. When exposure time is set to a constant value for all spectral bins, diffuse reflectance off a 1% absorbing material (Spectralon, Lab Sphere, North Sutton, NH) shows a peak at 740 nm. Total

number of counts on the sensor are then decrease up to 4.5-fold for both tails of the spectra at 580 and 950 nm. Therefore, exposure time at spectral bins with lower throughput needs to be increased to enhance SNR. It is worth mentioning that refresh rate of the DMD needs to be adjusted accordingly in the case of sinusoidal illumination. Another optimization on the system can be replacing the diffuser which was installed to homogenize the beam profile with a light pipe homogenizing rod (48-582, Edmund Optics, Barrington, New Jersey). The Quantum Efficiency (QE) of the camera at wavelengths higher than 900 nm is below 25% as compared to 82% at around 580 nm. All the lenses in the proposed optical configuration have Anti-Reflection (AF) coating in the 650-1000 nm range. Achieving high SNR at wavelengths higher than 900 nm can be important to decouple absorption contribution of fat and water in biological tissue which have peaks at 930 and 970 nm respectively.

The proposed slit-scanning approach provides flexibility in selecting the bandwidth and central wavelength of supercontinuum source even outside our current operating spectral range, 580-950 nm, e.g. short-wave infrared (900-1700 nm). However, we believe the slit-scanning approach decreases a large portion of light throughput by passing the input beam through multiple lenses. Another wavelength-tuning approach is to integrate an Acousto-Optic Tunable Filter (AOTF) to the system. This component uses birefringent features of a Chrystal such as tellurium dioxide under Radio Frequency (RF) input to modulate the Chrystal's refractive index, thus tuning wavelength of input beam [69].

3.5 Conclusion and Future Work

In conclusion, we demonstrated integration of a versatile wavelength-tuning configuration to a supercontinuum laser as part of the projection unit for a hyperspectral SFDI instrument to record tissue optical properties over 1000 wavelength bands (from 580 to 950 nm). We validated the

performance of the hs-SFDI instrument to quantity and decouple optical properties, absorption and reduced scattering, in a range of tissue simulating phantom by comparing absorption values to spectrophotometer measurements. Average absorption values were within 6.7% of the spectrophotometer data. Reduced scattering coefficients were within 20.4% of analytical model from Mie theory. The effect of wide spectral range and fine spectral resolution was shown by measuring a tissue phantom consisting of 4 wells with distinct spectral signatures. We also performed an ex-vivo measurement of a beef sample to quantify and spatially resolve spectral fingerprints of a variety of tissue-constituting molecules such as oxy- deoxy- and met- hemoglobin as well as water and fat.

While there are challenges in accelerating image acquisition on the hs-SFDI system, techniques such as integration to single pixel SFDI techniques [50] and encoding hyperspectral information in the illumination beam via Light Labeling [33, 64] have potentials to resolve the trade-off between spectral and temporal resolution.

Despite these challenges, our study provides a platform to characterize and localize tissue structure and constituents with mm resolution over a scalable field of view using quantitative continuous hyperspectral optical-property content with implications to monitor pathologic and physiologic states.

Chapter 4

4.   Compressed sensing Spatial Frequency Domain Imaging (cs-SFDI)

This chapter is derived from the publication [50].

4.1   Introduction

Spatial Frequency Domain Imaging (SFDI) is a non-contact wide-field imaging technique that employs sinusoidal patterns of intensity-modulated light to characterize multiply scattering media, such as biological tissue. SFDI separates the contributions of light scattering from absorption by measuring the frequency-dependent modulation transfer function of diffusively reflected structured light. This information is used to map and form images of tissue optical parameters μ'_s and μ_a, respectively [14, 15]. Optical properties at multiple wavelengths are used to derive quantitative images of biochemical composition, such as the tissue concentration of oxy and deoxyhemoglobin and water. SFDI techniques have been utilized widely to characterize tissue composition and function in humans [18, 19], animal models, and *ex vivo* tissue specimens [70, 71].

There is generally a tradeoff between spectral and spatial information content in SFDI instruments. This is due to the fact that wide-field imaging is typically performed serially at several discrete wavelengths using selective illumination and/or optical filters [14, 72]. Spatial frequency domain spectroscopy (SFDS) was introduced to enhance spectral content using a broadband light source, fiber-based collection, and a spectrometer [73, 74]. However, this approach has a Field-of-View (FOV) that is limited to the collection fiber (~ 2 mm). Hyperspectral imaging cameras can expand the FOV, however these systems are generally relatively expensive and can have limitations in speed, dynamic range, and sensitivity [46, 75]. In this letter we describe an alternative approach that incorporates compressed sensing (CS) and a single pixel detector for wide-field multi-spectral

imaging. This strategy is compatible with both broadband light sources imaged with fiber-coupled spectrometers and single element detectors using several temporally-encoded wavelengths/sources.

Imaging applications of CS were first introduced in a "single pixel camera" form factor that transferred workload from hardware to post acquisition computation [65]. CS addresses image reconstruction by relying on random samples from a scene under view instead of capturing individual pixels. This approach can be particularly effective in NIR and SWIR spectroscopic imaging by replacing expensive cameras with a single photodetector [76]. In addition, resolution requirements for SFDI mapping of μ'_s and μ_a are determined by the relatively low frequency of variations in the tissue transport scattering length ($l_{tr} \sim 1$ mm). This allows typical SFDI sinusoidal projection patterns to sample tissue sparsely at $f \sim 1/(3l_{tr})$ [14, 77]. Since CS methods utilize principles of sparsity, the number of random samples imposed by Nyquist Shannon boundary can be reduced and CS is well-matched with diffuse optical imaging and tomography [78, 79]

4.2   Materials and Methods

4.2.1   Spatial Frequency Domain Imaging

The SFDI instrumentation, data acquisition and post-processing have been previously enumerated elsewhere [14]. Briefly, spatially modulated light is projected onto a sample via a Digital Light Processing (DLP) unit. At each spatial frequency, three evenly spaced modulation phases of 0°, 120° and 240° are cycled through. The diffusively reflected light is then captured with a camera. The phase-offset images are next fed in a three-phase demodulation formula, Equation 4-1, to extract spatial frequency dependent reflectance. The demodulated reflectance is also calibrated to account for instrument function. As it was shown in [14], the reflectance sensitivity to optical absorption and scattering varies as a function of spatial frequency. This can be modeled with

diffusion theory or Monte Carlo simulations. Using a minimum of two spatial frequencies, the calibrated reflectance at every pixel is then applied to the simulations resulting in μ'_s and μ_a maps. Once the μ'_s and μ_a are decoupled at several wavelengths, μ_a is used to calculate hemodynamic parameters by assuming that oxy/deoxyhemoglobin and water are the dominant absorbing chromophores in the medium.

$$AC(x,y) = \frac{2^{1/2}}{3}\{[I_{0°}(x,y) - I_{120°}(x,y)]^2$$
$$+ [I_{120°}(x,y) - I_{240°}(x,y)]^2$$
$$+ [I_{240°}(x,y) - I_{0°}(x,y)]^2\}^{1/2}$$

<div style="text-align:right">Equation 4-1</div>

4.2.2 Compressed Sensing Framework

Nyquist-Shannon is a fundamental sampling theorem in digital signal processing which states that a signal can exactly be recovered if the sampling rate is at least twice its highest frequency. Considering a 2D array with N pixels on a digital camera sensor, the raw image can be considered as vector $x[i], i = 1, 2, ..., N$. This vector can be expanded as a combination of its orthonormal basis such as discrete cosine transform, wavelet, etc. as shown in Equation 4-2.

$$x = \sum_{i=1}^{N} \Psi_i C_i$$

<div style="text-align:right">Equation 4-2</div>

Where $C_{i=1:N}$ and $\Psi_{i=(1:N)\times(1:N)}$ are the coefficient vector and transform operator, respectively. In the case of k-sparse expansion of x vector, only k number of C_i coefficients are non-zero. The compressed sensing technique [65] suggests using only $M << N$ ($M \approx k$) samples of the signal x with sensing matrix $\Phi_{i=(1:M)\times(1:N)}$ which gives the measurement vector as shown in Equation 4-3

$$y = \Phi x \qquad \text{Equation 4-3}$$

This rewrites Equation 4-2 as

$$y = \Phi \Psi C \qquad \text{Equation 4-4}$$

The sensing matrix Φ is independent of the raw image, x. As part of the compressed sensing algorithm, a convex optimization problem is solved using l_1-minimization to recover image x based on measurement vector y:

$$\hat{C} = argmin \|C\|_1 \text{ in a way that } \Phi \Psi C = y \qquad \text{Equation 4-5}$$

The raw image can then be reconstructed with $\hat{x} = \Psi \hat{C}$. In this paper, we have utilized the Denoising-based AMP (D-AMP) compressed sensing algorithm and source code developed in [80] on the post-processing side.

4.2.3   cs-SFDI

On the detection side of our cs-SFDI instrument, a sample, e.g. tissue phantom, is imaged via a collection lens onto a Digital Micro-Mirror Device (DMD) (CEL5500, Digital Light Innovation, Austin, TX) with N mirror bins. The sensing matrix Φ is also uploaded to the DMD memory as a stack of random patterns from a Bernoulli distribution [81]. This binary sensing matrix matches well with the ON/OFF orientation of the DMD. The reflected light from the DMD is then focused on the photodetector (DET100A, Thorlabs, Newton, NJ) and finally builds the measurement vector y. The compressed sensing algorithm allows for reducing the number of sampling patterns stored on a DMD to effectively reconstruct an image. This approach reduces both the duration of data acquisition and the cost of the DMD. Figure 4.1 shows a schematic of our cs-SFDI setup. On the excitation side, the output of three co-aligned LEDs (M660L4, M850L3, and M940L3, Thorlabs,

Newton, NJ) is condensed onto a sinusoidal-patterned mask (Applied Image Inc., Rochester, NY) and then the mask is imaged onto the tissue simulating phantom. The LEDs are simultaneously intensity-modulated in the frequency range of 3 kHz to 5 kHz which is higher than the sampler DMD's refresh rate. The reflected power of the frequency-encoded sources is determined for each random pattern via temporal frequency domain analysis. This feature is important because the high dynamic range of the photodetector enables adding more frequency-encoded light sources to the setup without affecting the total acquisition speed.

A LABVIEW platform (National Instruments, Austin, TX) controls the linear stage (T-LS28M, Zaber Technologies Inc, Vancouver, BC), the sampler DMD, and the photodiode, thus accelerating the data acquisition. In this configuration, we used a sinusoidal mask on a linear stage instead of a second DMD to project structured light [82, 83]. This was due to fact that each of the DMD array elements flickers on and off to generate grayscale intensities. In a camera based SFDI system, the camera's exposure time can be adjusted to match the Pulse Width Modulation (PWM) on the DMD. However, this can be problematic in a single pixel imager because of the photodiode's high bandwidth and lack of access to the PWM sequence of every single micro-mirror element. An addition advantage to transmission-based masks for SFDI is their low-cost and simplicity.
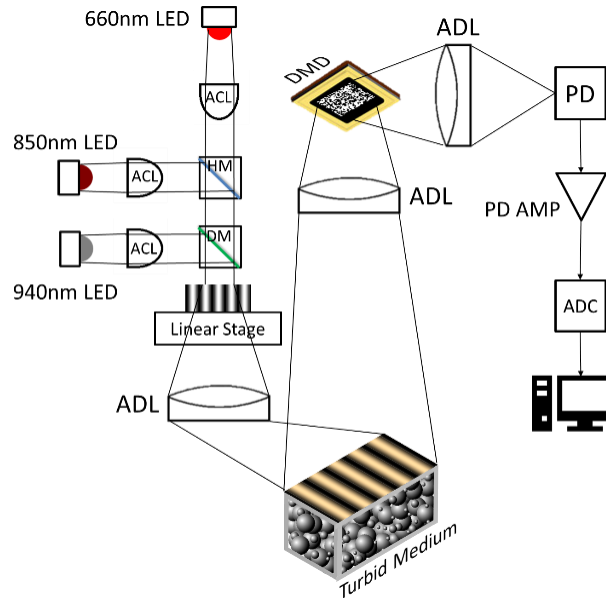
Figure 4.1 Schematic of the cs-SFDI instrument. DMD: Digital Micro-Mirror Device, PD: Photodiode, PD AMP: Photodiode Amplifier, ADC: Analog to Digital Converter, HM: Hot Mirror, DM: Dichroic Mirror, ACL: Aspheric Condenser Lens, ADL: Achromatic Doublet Lens.

4.3   Tissue phantom measurements

Tissue phantoms were used to investigate the ability of the compressed SFDI instrument to estimate bulk optical properties. The two phantoms of known optical properties were used here [16]. The absorption coefficient in these phantoms ranged from 0.015 to 0.03 mm−1 and the reduced scattering coefficient ranged from 0.5 to 1.5 mm−1 in the visible and near infrared spectra. The optical properties were measured using a frequency domain photon migration (FDPM) system, considered as our gold-standard [57]. We measured the bulk optical properties of these phantoms at 720, 780, 850, and 900 nm with the compressed SFDI instrument. The spatial frequency on the sample was set to 0.1 mm^{-1}. Figure 4.2 shows a comparison between tissue phantom's known optical properties and those recovered with the compressed SFDI instrument. Each point corresponds to a mean optical property from a 30 mm × 30 mm Region of Interest (ROI) on a reconstructed map at the mentioned wavelengths. The error bars are calculated from the standard deviation of the values on the same ROI. The average percent difference between the known

properties and the ones extracted using the proposed instrument were 6.4% and 1.3% for μ_s' and μ_a, respectively. The average relative standard deviation in μs' was 0.026 over the ROI using the compressed SFDI system. This parameter was 0.052 for the μ_a. These plots overally show good agreement of the bulk optical properties extraction using the proposed technique.
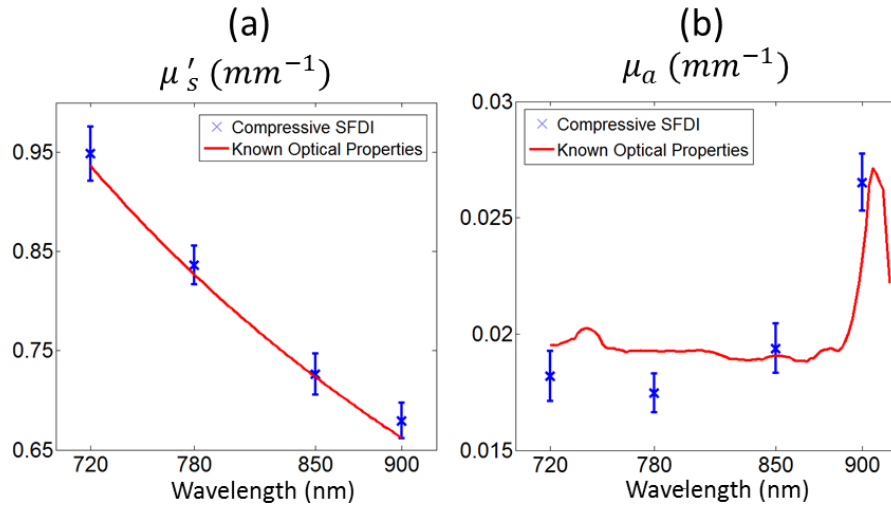
Figure 4.2 (a) Reduced scattering coefficient at four near infrared wavelengths: compressed SFDI vs known optical properties. (b) Absorption coefficient: compressed SFDI vs known optical properties.

We constructed tissue phantoms to investigate the ability of the cs-SFDI instrument to estimate bulk optical properties [57]. The "sample" phantom consists of a near-infrared absorbing lesion made of Naphthol Green B dye embedded in the central region of the PDMS base to produce spectral/spatial contrast. The central lesion has a lower concentration of scattering agent than the surrounding region. Figure 4.3 shows the work flow of the SFDI technique based on the images reconstructed with the cs-SFDI instrument. In Figure 4.3(a), the reflectance from phase-shifted sinusoidal projections is first captured by the compressed single pixel camera. These raw images are then demodulated to AC and DC components, Figure 4.3(b), calibrated against another tissue

phantom with known optical properties, Figure 4.3(c), and finally interpolated pixel by pixel to generate the µ'$_s$ and µ$_a$ maps, Figure 4.3(d).
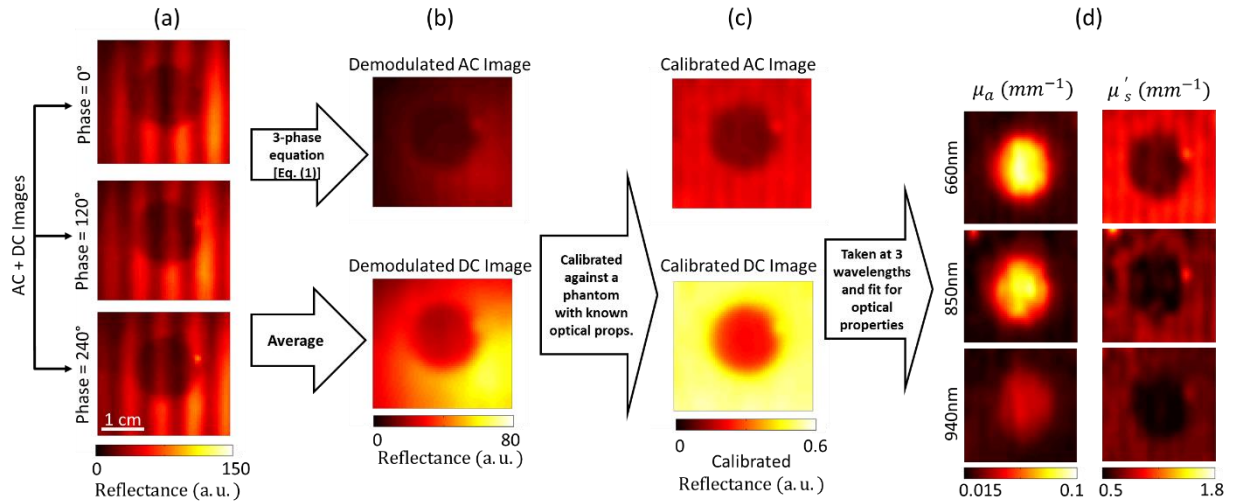
Figure 4.3 (a) Raw reflectances from the tissue phantom reconstructed with the single pixel detector. (b) Demodulated AC and DC reflectance (c) Calibrated Demodulated Reflectance (d) Absorption and reduced scattering coefficient maps at three wavelengths.

We compared cs-SFDI derived optical properties to those obtained with a conventional camera-based SFDI measurement. In the latter case, we replaced the cs-SFDI photodiode with a CCD camera (Flea3 1394B, Point Grey, Richmond, BC) and set all DLP mirrors to ON status. The three LEDs were serially controlled for each sinusoidal pattern projection to achieve spectral and spatial content. Figure 4.4(a) shows good agreement of the extracted bulk optical properties with the single pixel detector and the CCD camera on two contrasting regions of the phantom, the central lesion and the surrounding area. The average percent difference between these two imaging configurations were 7.6% and 4.3% for µ'$_s$ and µ$_a$, respectively. Each point in Figure 4.4(a) corresponds to a mean optical property from a 10 mm × 10 mm Region of Interest (ROI) on a reconstructed map at a specific wavelength. The error bars are calculated from the standard deviation of the values on the same ROIs. According to Figure 4.4(b), the absorption coefficient

of the central lesion follows the absorption spectra trend of Naphthol Green B while it remains

almost unchanged on the surrounding PDMS background. The reduced scattering coefficients also

follow the expected spatial contrast and power law dependence.
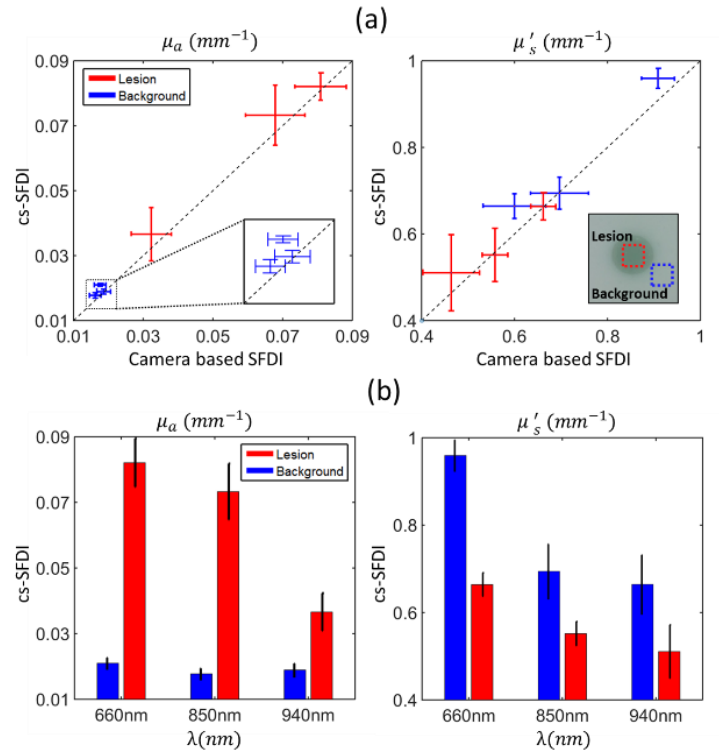
Figure 4.4 Bulk optical property measurements. (a) Comparison of bulk μ_a (Top Left) and μ'_s (Top Right) using standard camera based SFDI and cs-SFDI calculated at multiple wavelengths at two distinct regions of a tissue phantom: Background and Lesion (Tagged in a white light image of the phantom). (b) Spectral and spatial contrast in phantom's bulk μ_a (Bottom Left) and μ'_s (Bottom Right) extracted using the cs-SFDI instrument.

4.4   Sampling rate effect on image quality:

We first measured a highly scattering scene to test the quality of reconstructions on the single pixel

imager. The source here is a planar broadband illumination. Herein, the Sampling Rate (SR) is

defined as the number of random patterns, M, to the total number of image pixels, N.

Figure 4.5 shows the reconstructed 64×64 images with increase in the sampling rates. This is

followed by the PSNR-SR plot, which matches with the trends observed in [80]. It is worth

mentioning that near infrared is the scattering dominated regime in which tissue diminishes the high frequency components of the reflected image. Therefore, lower sampling rates can also be effective, resulting in a faster data acquisition.
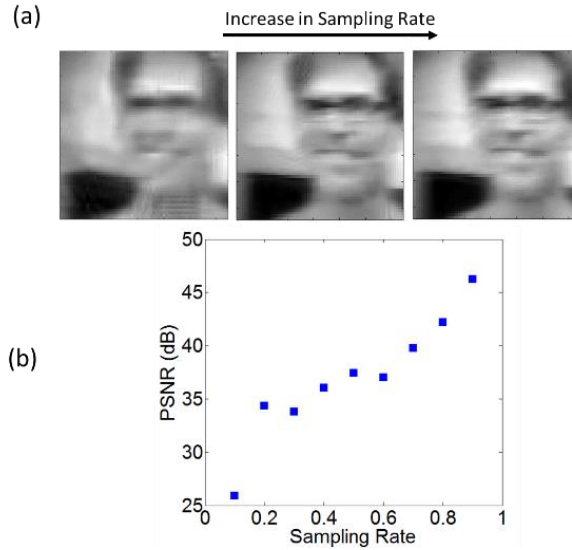
Figure 4.5 (a) Increase in image quality occurs with increase in sampling rate. (b) PSNR vs Sampling rate plot

4.5   Wavelength Encoding on the CS camera

We have done a preliminary study on simultaneous encoding of two wavelengths in time on the projections side of the CS Camera. In this configuration, two LEDs of specific wavelengths are modulated at distinct frequencies. On the detection side, a high bandwidth photodiode captures the signal for every random pattern generated on the DMD. Performing a FFT for each pattern-dependent signal separates the spectral components. The power of each component is finally calculated, resulting in a simultaneous recovery of the images at these two wavelengths. The images are reconstructed for a 660nm and 850nm LED modulated at 2.5 kHz and 4 kHz, ,respectively (Figure 4.6(a) and Figure 4.6(b)).
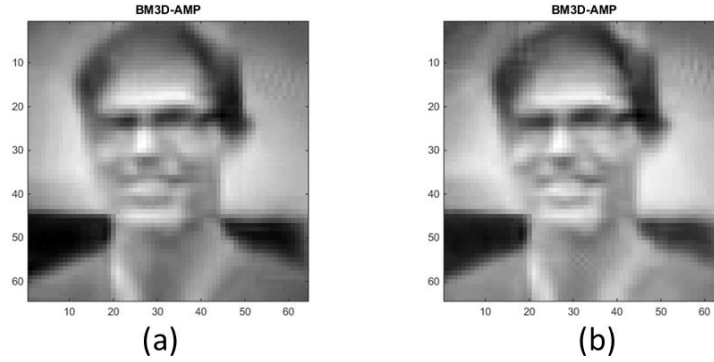
Figure 4.6 (a) Reconstructed image for the 660nm LED modulated at 2.5 kHz (b) Reconstructed image for the 850nm LED modulated at 4 kHz. The image resolution is 64×64 pixels and the sampling rate is set 0.2

4.6   Spectrometer-based cs-SFDI

To increase spectral resolution of proposed cs-SFDI instrument, the multi-LED light source can be replaced with a broadband light source, a 250 W Quartz Tungsten Halogen source (Newport Oriel, Irvine, CA, model 66883) with a temporal power stability unit (Newport Oriel, Irvine, CA, model 68950). The output of this light source is imaged onto a sinusoidal mask that is mounted on a linear stage and projected onto the tissue phantom, a reconstruction DMD toggles through random binary patterns and focuses the output of each pattern to the entrance slit of a tunable grating spectrograph (Newport Oriel, Irvine, CA, model 77480). **Error! Reference source not f ound.** (a) shows schematic of Spatial Frequency Domain Spectroscopy instrument [73] which is the single spot analogy of our proposed wide-field compressed sensing instrument. **Error! R eference source not found.** (b) shows a schematic of the spectrometer-based cs-SFDI instrument. Based on the procedure explained in section 4.2.3, a hyperspectral cube for absorption and reduced scattering maps can be generated. We measured a silicone-based tissue phantom with Naphthol Green B lesion in the middle and extracted absorption and reduced scattering at 85 spectral bins in the 500-875nm range. The number of spectral bins can be as large the number of pixels in the liner array detector. On this measurement, we binned pixels together to increase SNR. There is also a tradeoff between the spectral resolution of the spectrometer and entrance slit size which is

proportional with light throughput. Figure 4.8 shows bulk μ_a and μ'_s spectra at two ROIs, on the central lesion and the background, on the tissue phantom. The lesion shows higher absorption close to the peak of the Naphthol Green b absorption at 730nm. The concentration of the scattering agent, TiO2, is lower at the central lesion, therefore lower scattering values are extracted using the cs-SFDI instrument. One of the limitations with our spectrometer-based cs-SFDI instrument is low light throughput which led us to increase the exposure time
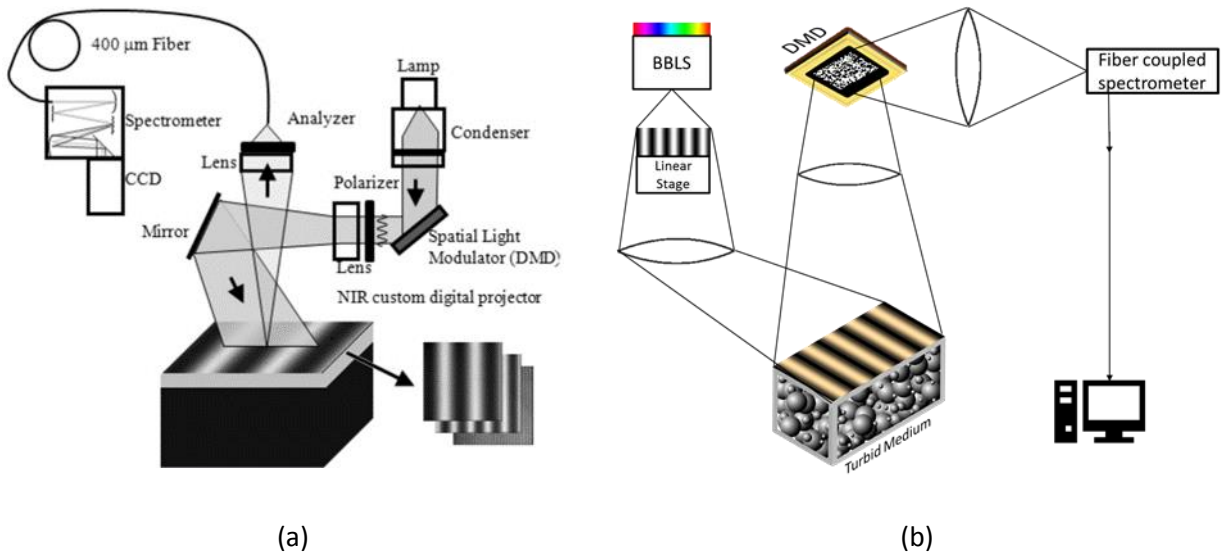

(a) (b)

Figure 4.7 (a) Schematic of spatial frequency domain spectroscopy (b) Schematic of spectrometer-based compressed sensing spatial frequency domain imaging
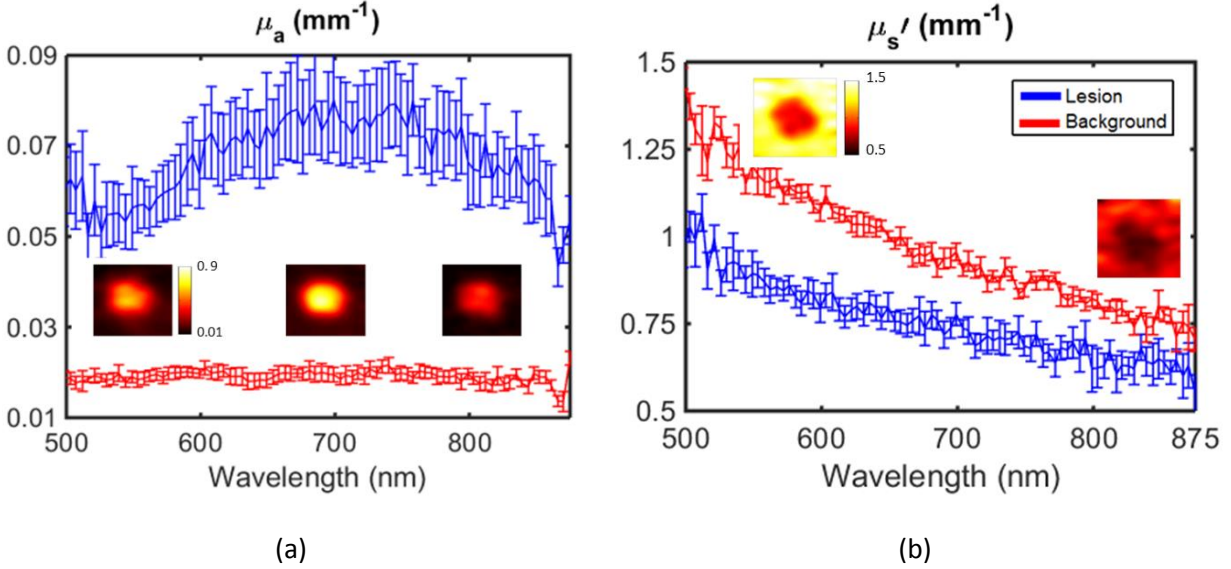
Figure 4.8 Bulk optical property measurements of tissue phantom using spectrometer-based cs-SFDI instrument. Two ROIs are chosen, one at center of the lesion and the other on the background. (a) bulk μ_a spectra and (b) bulk μ'_s spectra

4.7 Discussions

One of our primary goals in SFDI instrument development is to increase the data acquisition rate which mainly relies on three parameters: image resolution, number of phase shifted patterns, and number of wavelengths. From the perspective of the single pixel camera, higher image resolution requires increasing the number of sampling patterns on the DMD to achieve a certain accuracy of reconstruction. We have chosen our optimum image resolution based on the transport scattering length in tissue (l_{tr}) which is typically ~1 mm in the NIR. Thus, for 64×64 pixels in a 35 mm × 35 mm field of view, the pixel size is about 0.55 mm which is adequate and comparable to l_{tr}. A sampling rate of about 10%, i.e. 400 samples, is adequate for a tissue phantom illuminated with sinusoidal patterns at a spatial frequency of 0.1 mm^{-1}. This sampling rate results in a maximum acquisition rate of 12.5 Frames Per Second (FPS) on our DMD. However, other DMD chips, such as DLP7000 (Texas Instruments, Dallas, TX) provide refresh rates of 32550 Hz and acquisition rates of up to 80 FPS. Because cs-SFDI employs high-bandwidth single pixel detectors, spectral content can be increased using frequency encoding without reductions in image acquisition speed.

55

In the current cs-SFDI configuration, the linear translational stage used for shifting the sinusoidal phase pattern is a limiting factor in achieving higher frame rates and switching between multiple spatial frequencies. As a result, it takes 5 seconds in total to switch between 3 phase-shifted frames and capture images. Recently, signal processing techniques in the SFD have been developed to reduce the number of phases required to achieve the demodulated reflectance and achieve "single snapshot" performance [47, 48]. These methods, however, require a high number of cycles in the modulation pattern to avoid ringing artifacts [47]. This imposes faster sampling rates to preserve higher frequency content in the image, thus increasing acquisition time. Therefore, further studies are required to evaluate the fidelity and performance of the cs-SFDI system when using single snapshot demodulation techniques.

4.8   Conclusion

In conclusion, we have developed a single-pixel compressed sensing method for quantitative imaging of optical properties in the spatial frequency domain. A CS algorithm was used to decrease the size of the sensing matrix required to accurately reconstruct and map optical properties. Performance was validated using tissue-simulating phantoms and demonstrating agreement in absorption and reduced scattering coefficients between cs-SFDI and a conventional camera-based system. When combined with temporal encoding of multiple sources, cs-SFDI takes advantage of the high-bandwidth of single pixel detectors and provides a fixed frame rate strategy for simultaneous multi-spectral imaging. Future work will emphasize increasing imaging speed and spectral content by incorporating single-snapshot demodulation strategies, broadband light-labeling [64], and single-pixel, fiber-coupled spectrometer detection. These results provide a new framework for broadband multi- and hyper-spectral functional tissue imaging with important

implications for accurately and dynamically characterizing tissue composition, structure, and metabolism.

Chapter 5

5. Future Directions: Integration of Time of Flight cameras to Spatial Frequency Domain Imaging Instruments

One of the main challenges in measuring biological tissue using SFDI is the curvature of the sample. The raw intensity values of the sample at once calibrated against a tissue phantom appear to have lower values at steep angles as compared to "flat" surfaces. This phenomenon can mislead the Monte Carlo model of photon transport to assign higher absorption, lower scattering, or a combination of optical properties that are not true representative of the sample. The other challenge with similar behavior is the effect of height mismatch between the calibration phantom and biological sample. As tissue distance from the camera increases, calibrated reflectance values decrease which again can distort optical property fitting procedures. Therefore, couple of studies has been done to correct for the effect of surface curvature using structured illumination [84-86] and achieved curvature corrections up to 75°. Structured illumination techniques provide high spatial resolution via using DLP projectors and high definition cameras, they suffer from ambient light effects, can be expensive for certain models [87], and may require computationally intensive operations for quantitative extraction of depth data in the SFDI case. Figure 5.1 shows 3D profile of a human subject with RGB image and oxygen saturation maps overlaid on top. At steep angles and areas where shadows are present, close to the nose and mouth area, the profilometry algorithm did not operate well and masked the profile in black.

<div align="center">(a)   (b)</div>
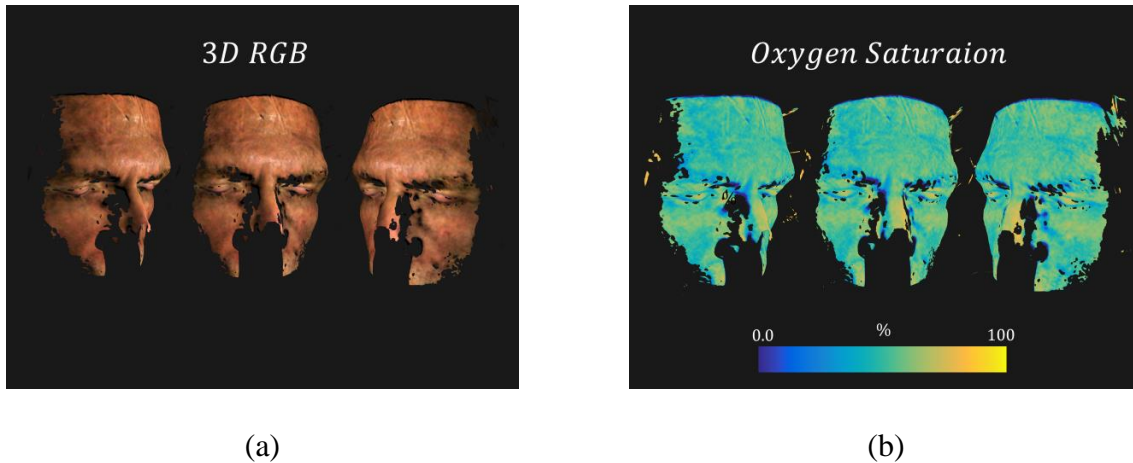
Figure 5.1 (a) Example of 3D topography based on structured illumination technique using Modulated Imaging Ox Imager Instrument (b) Overlaying of tissue oxygen saturation map on 3D profile

A competing technology for depth measurement which can be implemented to SFDI is Time of Flight (ToF) camera technology. A ToF camera calculates the phase delay between illumination of a pulsed or CW modulated source and reflection from a sample. The phase delay is then translated to distance, Figure 5.2(a). More details on the theory behind the ToF camera technology can be found in [87]. We have chosen a 3D ToF sensor evaluation module (OPT8241, Texas Instruments, Austin, USA), shown in Figure 5.2 (b) to investigate the feasibility of extraction distance/angle-corrected optical properties in real-time using the SFDI technique. The operating wavelength of the illumination source is 850 nm, modulation frequency of the source is in the 10-100 MHz range, camera resolution is 320×240 pixels and maximum frame rate is 60 FPS. One of the advantages with modulated source in the MHz regime is canceling room light artifact which is a limitation in clinical measurements.

(a)   (b)
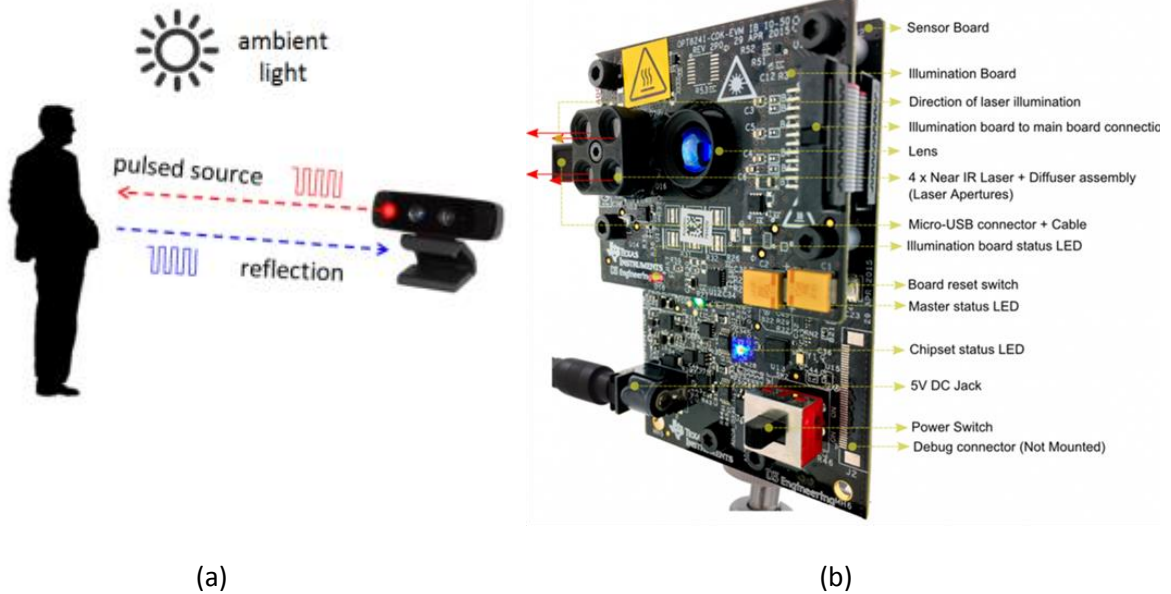
Figure 5.2 (a) 3D ToF camera operation (b) Texas Instruments OPT 8241 ToF evaluation module [88]

We first measured a cylindrical tissue phantom placed in front of a flat phantom. The ToF module is then used to extract intensity and depth of the samples. Once the depth is determined, raw intensity values are corrected based on geometric correction of the phantom's Lambertian diffuse reflectance [84]. Figure 5.3 shows the effect angle and distance correction on the cylindrical phantom and the flat phantom mounted behind it. The reference plane is assumed to be on the axis of the cylinder. Therefore, the farther plane, the flat phantom is modified to have higher intensity and closer planes, yellow regions in the raw intensity map, are modified to have lower intensity. The Lambertian correction used for intensity-correction of regions at an angle, correction factors at angles larger than 70° which results in larger intensity values at these regions.
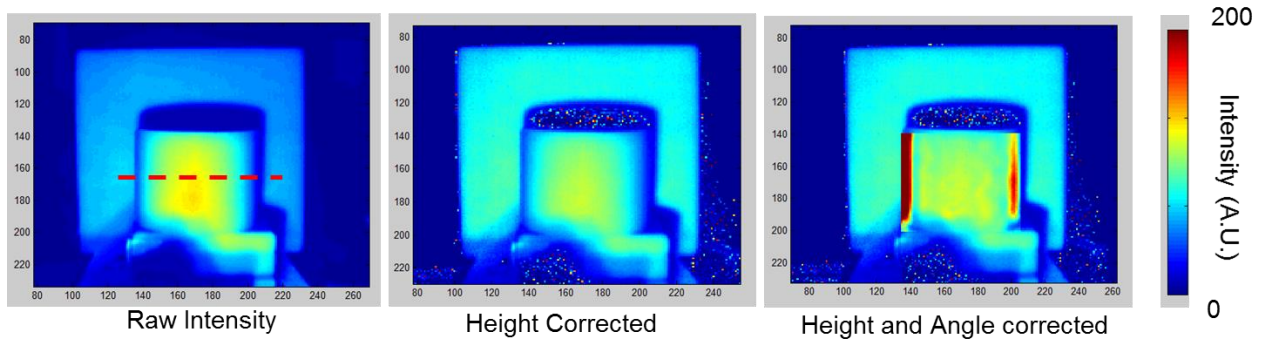
Figure 5.3 Correction for angle and depth of tissue phantoms using the ToF camera module

Figure 5.4 shows the effect of height correction and height/angle correction on the intensity of the cylindrical phantom. As it was mentioned, the reference plane is considered on the central axis of the cylinder, therefore less correction is implemented on two sides of the intensity curve as opposed to the apex.
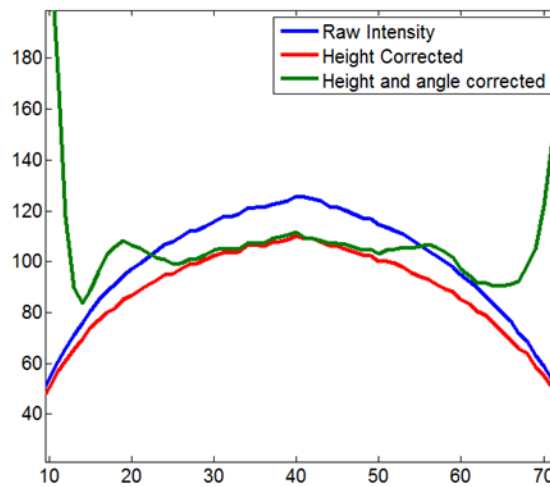
Figure 5.4 Intensity of a cross section of the cylindrical phantom: raw intensity; height corrected intensity; height/angle correction intensity

The ToF module can acquire simultaneous phase and intensity data at 60 FPS depending the operating mode (short range or long range) [88], we can take advantage of this high temporal resolution to extract high beat and respiration data from raw intensity maps. We imaged forearm of a human subject using the ToF camera, chose a ROI next to a vessel where it was assumed to show higher pulsatile fluctuations. We then performed FFT using Matlab's built-in function to

61

extract heart rate of the subject as shown in Figure 5.5 (a). More repeatability measurements can be done using pulsatile flow phantoms to validate the accuracy of heart rate extraction using the ToF sensor.
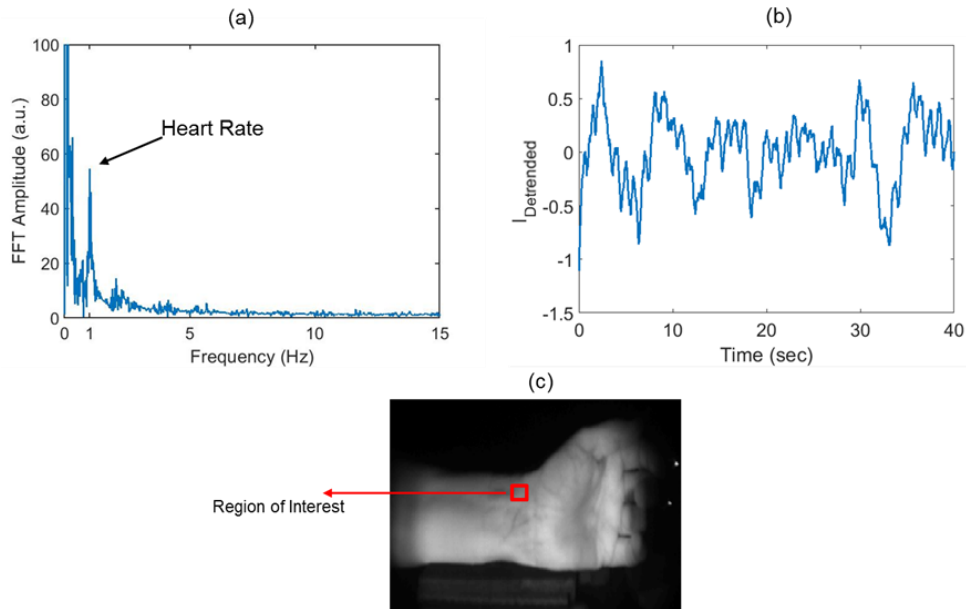
Figure 5.5 (a) FFT of intensity values form a ROI on a human's wrist (b) Time domain intensity fluctuations represent heart beat information (c) Reflectance image of the sample and the chosen ROI

We finally condensed the output of the temporally modulated light source onto a sinusoidal-patterned mask (Applied Image Inc., Rochester, NY) and then imaged the mask onto the forearm region. By mounting the mask on a linear stage, three evenly spaced modulation phases of 0°, 120° and 240° are cycled through. The diffusively reflected light is then captured with the ToF camera. Once the raw images are demodulated and calibrated against a tissue phantom with known optical properties, calibrated diffuse reflectance is fitted using a Montel Carlo model of photon transport in turbid medium to yield absorption and reduced scattering maps at 850 nm. Since, quantitative depth information is simultaneously acquired with the intensity values, a 3D profile map of the forearm with absorption coefficient overlaid on top can be extracted as shown in Figure 5.6.
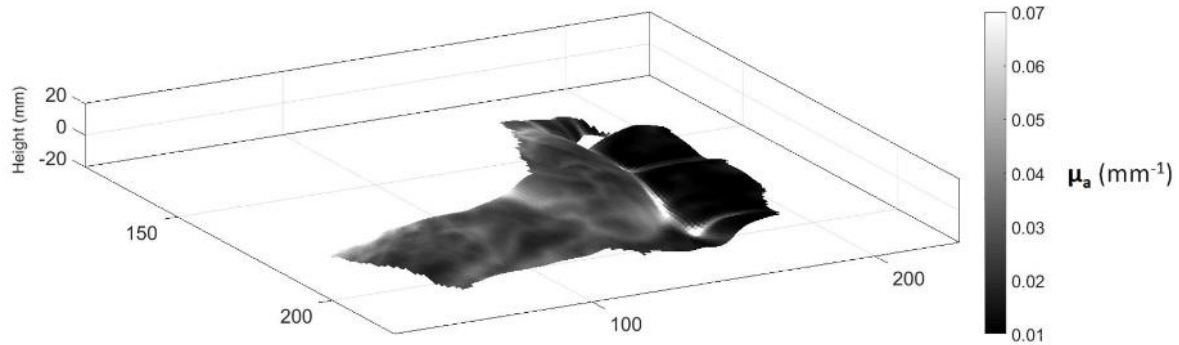
Figure 5.6 3D profile of forearm with absorption coefficient maps overlaid on top

The next generation of ToF enabled SFDI instrument can be based on using DMD projectors instead of the sinusoidal mask to achieve higher image acquisition rates. The maximum frame-rate on the ToF camera is 60 FPS. Using three phases of a specific spatial frequency, this frame rate to optical property extraction rates of 20 FPS for one wavelengths. Adding a modulated light source, preferably at wavelength of 66 nm, provides the ability to decouple oxy and deoxyhemoglobin concentrations at 10 Hz.

Another future direction in extracting quantitative phase information, in addition to measuring depth of a sample, is to switch between multiple source modulation frequencies in the MHz regime and utilize principles of frequency domain photon migration in turbid medium to quantify optical properties at several layers [12].

Chapter 6

6. Conclusions

The body of this work focus on instrumentation techniques to increase temporal and spectral resolution in Spatial Frequency Domain Imaging (SFDI) to meet requirements of certain tissue imaging studies. To mitigate the trade-off between spectral and temporal resolution, novel instrumentation and signal-processing techniques are utilized.

In **Chapter 2** of this thesis, we introduced a high speed SFDI instrument based on square wave projections, three wavelengths, and two spatial frequency. The instrument's acquisition rate, spatial resolution, working distance, field of view, and optomechanical design were based on considerations to match with a preclinical model of cardiac arrest and resuscitation. By acquiring SFDI data directly from the brain, the insrurment provides maps of cerebral absorption and scattering changes with high temporal resolution ($\sim$14 Hz). This enables characterization of rapid changes in tissue scattering properties that may be related to perturbations in structure and function of neurons and mitochondria, in addition to rapid hemodynamic changes due to ischemia and reperfusion.

The theme of **Chapter 3** was to introduce a hyperspectral SFDI (hs-SFDI) instrument by integrating a supercontinuum laser source to a wavelength-tuning optical configuration and pattern projection unit. Using a high-speed sCMOS camera, this system allowed us to calculate tissue phantom's optical properties, absorption and reduced scattering, over a 4 cm$\times$6 cm FOV at more than 1000 spectral bins. hs-SFDI performance is validated using tissue-simulating phantoms, spectrophotometer measurements, and Mie theory analytical models over a range of (μ_a) and (μ'_s) values. Quantitative hs-SFDI images were obtained from an ex-vivo beef sample in order to spatially resolve concentrations of oxy- deoxy- and met- hemoglobin as well as water

and fat fractions. Our results demonstrate that hs-SFDI can quantitatively image tissue optical properties with 1000 spectral bins in the 580-950 nm range over a wide, scalable Field-of-View (FOV). With an average of accuracy of 6.7% in μ_a and 20.4% in μ'_s compared to spectrophotometer results and Mie theory, respectively, hs-SFDI offers a promising approach for quantitative hyperspectral tissue optical imaging.

In each of the previous chapters, one aspect of temporal or spectral resolution was compromised. Demonstrated in **Chapter 4** of this thesis, to mitigate the trade-off between spectral and temporal resolution, we developed compressed sensing single pixel spatial frequency domain imaging (cs-SFDI) to characterize tissue optical properties over a wide field of view (35 mm × 35 mm) using multiple near-infrared (NIR) wavelengths simultaneously. Our approach takes advantage of the relatively sparse spatial content required for mapping tissue optical properties at length scales comparable to the transport scattering length in tissue (l tr ~ 1 mm) and the high bandwidth available for spectral encoding using a single-element detector. cs-SFDI recovered absorption and reduced scattering coefficients of a tissue phantom at three NIR wavelengths (660, 850, and 940 nm) within 7.6% and 4.3% of absolute values determined using camera-based SFDI, respectively. These results suggest that cs-SFDI can be developed as a multi- and hyperspectral imaging modality for quantitative, dynamic imaging of tissue optical and physiological properties.

7.   References

1.   Iftimia, N., W.R. Brugge, and D.X. Hammer, *Advances in Optical Imaging for Clinical Medicine*. Vol. 6. 2011: John Wiley & Sons.

2.   Kalani, M., et al., *Beneficial effects of dalteparin on haemostatic function and local tissue oxygenation in patients with diabetes, severe vascular disease and foot ulcers.* Thrombosis research, 2007. **120**(5): p. 653-661.

3.   Werner, C. and K. Engelhard, *Pathophysiology of traumatic brain injury.* British journal of anaesthesia, 2007. **99**(1): p. 4-9.

4.   Yazdi, H.S., et al., *Mapping breast cancer blood flow index, composition, and metabolism in a human subject using combined diffuse optical spectroscopic imaging and diffuse correlation spectroscopy.* Journal of biomedical optics, 2017. **22**(4): p. 045003.

5.   Huang, Y., et al., *An optical probe for detecting chondrocyte apoptosis in response to mechanical injury.* Scientific Reports, 2017. **7**(1): p. 10906.

6.   Li, S., et al., *Hyaluronic Acid-Based Optical Probe for the Diagnosis of Human Osteoarthritic Cartilage.* Nanotheranostics, 2018. **2**(4): p. 347.

7.   Magnusson, R., et al. *The guided-mode resonance biosensor: principles, technology, and implementation*. in *Frontiers in Biological Detection: From Nanosensors to Systems X*. 2018. International Society for Optics and Photonics.

8.   Hemmati, H., Y.H. Ko, and R. Magnusson, *Fiber-facet-integrated guided-mode resonance filters and sensors: experimental realization.* Optics letters, 2018. **43**(3): p. 358-361.

9.   Lee, K., et al., *Near-Infrared Fluorescence Modulation of Refolded DNA Aptamer-Functionalized Single-Walled Carbon Nanotubes for Optical Sensing.* ACS Applied Nano Materials, 2018.

10.   Patterson, M.S., B. Chance, and B.C. Wilson, *Time resolved reflectance and transmittance for the noninvasive measurement of tissue optical properties.* Applied optics, 1989. **28**(12): p. 2331-2336.

11.   Patterson, M.S., et al., *Frequency-domain reflectance for the determination of the scattering and absorption properties of tissue.* Applied optics, 1991. **30**(31): p. 4474-4476.

12.   Tromberg, B.J., et al., *Non–invasive measurements of breast tissue optical properties using frequency–domain photon migration.* Philosophical Transactions of the Royal Society of London B: Biological Sciences, 1997. **352**(1354): p. 661-668.

13.   Farrell, T.J., M.S. Patterson, and B. Wilson, *A diffusion theory model of spatially resolved, steady‑state diffuse reflectance for the noninvasive determination of tissue optical properties invivo.* Medical physics, 1992. **19**(4): p. 879-888.

14.   Cuccia, D.J., et al., *Quantitation and mapping of tissue optical properties using modulated imaging.* Journal of biomedical optics, 2009. **14**(2): p. 024012-024012-13.

15.   Cuccia, D.J., et al., *Modulated imaging: quantitative analysis and tomography of turbid media in the spatial-frequency domain.* Opt. Lett, 2005. **30**(11): p. 1354-1356.

16.   Lin, A.J., et al., *Spatial frequency domain imaging of intrinsic optical property contrast in a mouse model of Alzheimer's disease.* Annals of biomedical engineering, 2011. **39**(4): p. 1349-1357.

17.   Nadeau, K., et al., *Quantitative assessment of renal arterial occlusion in a porcine model using spatial frequency domain imaging.* Optics letters, 2013. **38**(18): p. 3566-3569.

18.   Saager, R.B., et al., *In vivo isolation of the effects of melanin from underlying hemodynamics across skin types using spatial frequency domain spectroscopy.* Journal of biomedical optics, 2016. **21**(5): p. 057001-057001.

19.   Gioux, S., et al., *First-in-human pilot study of a spatial frequency domain oxygenation imaging system.* Journal of biomedical optics, 2011. **16**(8): p. 086015-086015-10.

20.   Saager, R.B., et al., *Method for depth-resolved quantitation of optical properties in layered media using spatially modulated quantitative spectroscopy.* Journal of biomedical optics, 2011. **16**(7): p. 077002-077002-8.

21.   Weber, J.R., et al., *Multispectral imaging of tissue absorption and scattering using spatial frequency domain imaging and a computed-tomography imaging spectrometer.* Journal of biomedical optics, 2011. **16**(1): p. 011015.

22.   Singh-Moon, R.P., et al., *Spatial mapping of drug delivery to brain tissue using hyperspectral spatial frequency-domain imaging.* Journal of biomedical optics, 2014. **19**(9): p. 096003-096003.

23.   Nadeau, K.P., *High-speed, Quantitative Tissue Spectral Imaging in the Spatial Frequency Domain*, 2015, UC Irvine.

24.   Wilson, R.H., et al., *High-speed spatial frequency domain imaging of rat cortex detects dynamic optical and physiological properties following cardiac arrest and resuscitation.* Neurophotonics, 2017. **4**(4).

25.   Nadeau, K.P., et al., *Multifrequency synthesis and extraction using square wave projection patterns for quantitative tissue imaging.* Journal of biomedical optics, 2015. **20**(11): p. 116005-116005.

26.   Crouzet, C., et al., *Cerebral blood flow is decoupled from blood pressure and linked to EEG bursting after resuscitation from cardiac arrest.* Biomedical optics express, 2016. **7**(11): p. 4660-4673.

27.   Thorlabs, *Creating a Custom Multi-LED Source for Microscope Illumination.*

28. Rezaei, A.S. and H.E. Taha. *Computational Study of Lift Frequency Responses of Pitching Airfoils at Low Reynolds Numbers*. in *55th AIAA Aerospace Sciences Meeting*. 2017.

29. Taha, H.E. and A.S. Rezaei. *Unsteady Viscous Lift Frequency Response Using The Triple Deck Theory*. in *2018 AIAA Aerospace Sciences Meeting*. 2018.

30. Esfahanian, V., et al., *An efficient GPU implementation of cyclic reduction solver for high-order compressible viscous flow simulations.* Computers & fluids, 2014. **92**: p. 160-171.

31. Najdahmadi, A., A. Zarei-Hanzaki, and E. Farghadani, *Mechanical properties enhancement in Ti–29Nb–13Ta–4.6 Zr alloy via heat treatment with no detrimental effect on its biocompatibility.* Materials & Design (1980-2015), 2014. **54**: p. 786-791.

32. Ataei, M., A. Zarei-Hanzaki, and A. Shamsolhodaei, *Shape memory response and mechanical properties of warm deformed NiTi intermetallic alloy.* Materials Science and Engineering: A, 2017. **680**: p. 291-296.

33. Torabzadeh, M., et al. *hyperspectral characterization of tissue simulating phantoms using a supercontinuum laser in a spatial frequency domain imaging instrument*. in *Design and Quality for Biomedical Technologies XI*. 2018. International Society for Optics and Photonics.

34. Torabzadeh, M., et al., *Hyperspectral imaging in the spatial frequency domain with a supercontinuum source.* Submitted to Journal of Biomedical Optics, 2018. **24**(7).

35. Leavesley, S.J., et al., *Hyperspectral imaging fluorescence excitation scanning for colon cancer detection.* Journal of biomedical optics, 2016. **21**(10): p. 104003.

36. Kiyotoki, S., et al., *New method for detection of gastric cancer by hyperspectral imaging: a pilot study.* Journal of biomedical optics, 2013. **18**(2): p. 026010.

37.   Akbari, H., et al., *Hyperspectral imaging and quantitative analysis for prostate cancer detection.* Journal of biomedical optics, 2012. **17**(7): p. 076005.

38.   Bjorgan, A., M. Milanic, and L.L. Randeberg, *Estimation of skin optical parameters for real-time hyperspectral imaging applications.* Journal of biomedical optics, 2014. **19**(6): p. 066003.

39.   Dicker, D.T., et al., *Differentiation of normal skin and melanoma using high resolution hyperspectral imaging.* Cancer biology & therapy, 2006. **5**(8): p. 1033-1038.

40.   Randeberg, L.L., E.L.P. Larsen, and L.O. Svaasand, *Characterization of vascular structures and skin bruises using hyperspectral imaging, image analysis and diffusion theory.* Journal of biophotonics, 2010. **3**(1-2): p. 53-65.

41.   Vogel, A., et al., *Using noninvasive multispectral imaging to quantitatively assess tissue vasculature.* Journal of biomedical optics, 2007. **12**(5): p. 051604.

42.   Vasefi, F., et al., *Transillumination hyperspectral imaging for histopathological examination of excised tissue.* Journal of biomedical optics, 2011. **16**(8): p. 086014.

43.   Duann, J.-R., et al., *Separating spectral mixtures in hyperspectral image data using independent component analysis: validation with oral cancer tissue sections.* Journal of biomedical optics, 2013. **18**(12): p. 126005.

44.   Poh, C.F., et al., *Fluorescence visualization detection of field alterations in tumor margins of oral cancer patients.* Clinical Cancer Research, 2006. **12**(22): p. 6716-6722.

45.   Nandy, S., et al., *Characterizing optical properties and spatial heterogeneity of human ovarian tissue using spatial frequency domain imaging.* Journal of biomedical optics, 2016. **21**(10): p. 101402-101402.

46. Konecky, S.D., et al., *Hyperspectral optical tomography of intrinsic signals in the rat cortex.* Neurophotonics, 2015. **2**(4): p. 045003-045003.

47. Nadeau, K.P., A.J. Durkin, and B.J. Tromberg, *Advanced demodulation technique for the extraction of tissue optical properties and structural orientation contrast in the spatial frequency domain.* Journal of biomedical optics, 2014. **19**(5): p. 056013-056013.

48. Vervandier, J. and S. Gioux, *Single snapshot imaging of optical properties.* Biomedical optics express, 2013. **4**(12): p. 2938-2944.

49. Applegate, M.B. and D.M. Roblyer. *High-speed spatial frequency domain imaging with temporally modulated light*. 2017. SPIE.

50. Torabzadeh, M., et al., *Compressed single pixel imaging in the spatial frequency domain.* Journal of Biomedical Optics, 2017. **22**(3): p. 030501-030501.

51. Domingue, S.R., D.G. Winters, and R.A. Bartels. *Light labeling with temporal intensity modulations for hyperspectral imaging*. in *Imaging, Manipulation, and Analysis of Biomolecules, Cells, and Tissues IX*. 2016. International Society for Optics and Photonics.

52. van der Mark, M.B. and A. Desjardins. *Diffuse spectroscopy with very high collection efficiency*. in *CLEO: Applications and Technology*. 2011. Optical Society of America.

53. Nguyen, J.Q., et al., *Spatial frequency domain imaging of burn wounds in a preclinical model of graded burn severity.* Journal of biomedical optics, 2013. **18**(6): p. 066010-066010.

54. Yafi, A., et al., *Quantitative skin assessment using spatial frequency domain imaging (SFDI) in patients with or at high risk for pressure ulcers.* Lasers in surgery and medicine, 2017. **49**(9): p. 827-834.

55.   Najdahmadi, A., J.R. Lakey, and E. Botvinick, *Structural Characteristics and Diffusion Coefficient of Alginate Hydrogels Used for Cell Based Drug Delivery.* MRS Advances, 2018: p. 1-10.

56.   Pham, T.H., et al., *Broad bandwidth frequency domain instrument for quantitative tissue optical spectroscopy.* Review of Scientific Instruments, 2000. **71**(6): p. 2500-2513.

57.   Ayers, F., et al. *Fabrication and characterization of silicone-based tissue phantoms with tunable optical properties in the visible and near infrared domain.* in *Biomedical Optics (BiOS) 2008.* 2008. International Society for Optics and Photonics.

58.   Flock, S.T., et al., *Optical properties of Intralipid: a phantom medium for light propagation studies.* Lasers in surgery and medicine, 1992. **12**(5): p. 510-519.

59.   Michels, R., F. Foschum, and A. Kienle, *Optical properties of fat emulsions.* Optics Express, 2008. **16**(8): p. 5907-5925.

60.   Bland, J.M. and D. Altman, *Statistical methods for assessing agreement between two methods of clinical measurement.* The lancet, 1986. **327**(8476): p. 307-310.

61.   Filatova, S.A., I.A. Shcherbakov, and V.B. Tsvetkov, *Optical properties of animal tissues in the wavelength range from 350 to 2600 nm.* Journal of biomedical optics, 2017. **22**(3): p. 035009.

62.   Xia, J., et al., *Characterizing beef muscles with optical scattering and absorption coefficients in VIS-NIR region.* Meat Science, 2007. **75**(1): p. 78-83.

63.   Jacques, S.L., *Optical properties of biological tissues: a review.* Physics in Medicine & Biology, 2013. **58**(11): p. R37.

64.   Domingue, S.R., D.G. Winters, and R.A. Bartels, *Hyperspectral imaging via labeled excitation light and background-free absorption spectroscopy.* Optica, 2015. **2**(11): p. 929-932.

65.   Duarte, M.F., et al., *Single-pixel imaging via compressive sampling.* IEEE Signal Processing Magazine, 2008. **25**(2): p. 83.

66.   Wilson, R., et al., *A Multimodal Optical Imaging Platform that Predicts Neurological Recovery after Cardiac Arrest in an "Animal Neuro-Intensive Care Unit" (S42. 003)*, 2018, AAN Enterprises.

67.   Lin, A.J., et al., *Visible spatial frequency domain imaging with a digital light microprojector.* Journal of biomedical optics, 2013. **18**(9): p. 096007-096007.

68.   Valdes, P.A., et al., *qF-SSOP: real-time optical property corrected fluorescence imaging.* Biomedical optics express, 2017. **8**(8): p. 3597-3605.

69.   Kaur, P. and S. Kaur, *Acousto Optic Tunable Filters.* International Journal Of Electronics& Communication Technology, 2015. **6**(3): p. 64-67.

70.   Tabassum, S., et al., *Feasibility of spatial frequency domain imaging (SFDI) for optically characterizing a preclinical oncology model.* Biomedical Optics Express, 2016. **7**(10): p. 4154-4170.

71.   Laughney, A.M., et al., *Spectral discrimination of breast pathologies in situ using spatial frequency domain imaging.* Breast Cancer Research, 2013. **15**(4): p. 1.

72.   Saager, R., et al., *A light emitting diode (LED) based spatial frequency domain imaging system for optimization of photodynamic therapy of nonmelanoma skin cancer: quantitative reflectance imaging.* Lasers in surgery and medicine, 2013. **45**(4): p. 207-215.

73. Saager, R.B., D.J. Cuccia, and A.J. Durkin, *Determination of optical properties of turbid media spanning visible and near-infrared regimes via spatially modulated quantitative spectroscopy.* Journal of Biomedical Optics, 2010. **15**(1): p. 017012.

74. Saager, R.B., et al., *In vivo measurements of cutaneous melanin across spatial scales: using multiphoton microscopy and spatial frequency domain spectroscopy.* Journal of Biomedical Optics, 2015. **20**(6): p. 066005-066005.

75. Weber, J.R., et al., *Multispectral imaging of tissue absorption and scattering using spatial frequency domain imaging and a computed-tomography imaging spectrometer.* Journal of Biomedical Optics, 2011. **16**(1): p. 011015-011015-7.

76. McMackin, L., et al. *A high-resolution SWIR camera via compressed sensing.* in *SPIE Defense, Security, and Sensing.* 2012. International Society for Optics and Photonics.

77. O'Sullivan, T.D., et al., *Diffuse optical imaging using spatially and temporally modulated light.* Journal of Biomedical Optics, 2012. **17**(7): p. 0713111-07131114.

78. Süzen, M., A. Giannoula, and T. Durduran, *Compressed sensing in diffuse optical tomography.* Optics express, 2010. **18**(23): p. 23676-23690.

79. Provost, J. and F. Lesage, *The application of compressed sensing for photo-acoustic tomography.* IEEE transactions on medical imaging, 2009. **28**(4): p. 585-594.

80. Metzler, C.A., A. Maleki, and R.G. Baraniuk, *From denoising to compressed sensing.* 2014.

81. Baraniuk, R., et al., *A simple proof of the restricted isometry property for random matrices.* Constructive Approximation, 2008. **28**(3): p. 253-263.

82.   Guclu, C., et al. *Artificial magnetism via nanoantennas under azimuthally polarized vector beam illumination*. in *CLEO: Applications and Technology*. 2016. Optical Society of America.

83.   Zeng, J., et al. *Unveiling magnetic and chiral nanoscale properties using structured light and nanoantennas*. in *2017 11th International Congress on Engineered Materials Platforms for Novel Wave Phenomena (Metamaterials)*. 2017.

84.   Gioux, S., et al., *Three-dimensional surface profile intensity correction for spatially modulated imaging*. Journal of biomedical optics, 2009. **14**(3): p. 034045.

85.   Nguyen, T.T., et al., *Three-dimensional phantoms for curvature correction in spatial frequency domain imaging*. Biomedical optics express, 2012. **3**(6): p. 1200-1214.

86.   Zhao, Y., et al., *Angle correction for small animal tumor imaging with spatial frequency domain imaging (SFDI)*. Biomedical optics express, 2016. **7**(6): p. 2373-2384.

87.   Li, L., *Time-of-flight camera–an introduction*. Technical white paper, 2014(SLOA190B).

88.   Instruments, T., *OPT8241 Evaluation Module*, OPT8241 Quick Start Guide (SBOU156).